Journal of Controlled Release 394 (2026) 114903

Contents lists available at ScienceDirect

Journal of Controlled Release

journal homepage: www.elsevier.com/locate/jconrel

Biomimetic trident lipid anchoring enables stable neutrophil-based combination therapy

Luping Zhang [a,c], Yu Jin [a], Meixi Hao [a], Yijun Chen [a], Yupeng Dai [a], Mengtong Wu [a], Zihao Zhang [a], Tong Wu [a], Luyao Fang [a], Yujiao Wang [a], Xiao Xu [b,*], Caoyun Ju [a,*], Can Zhang [a,*]

[a] State Key Laboratory of Natural Medicines, Jiangsu Key Laboratory of Drug Discovery for Metabolic Diseases, Center of Advanced Pharmaceuticals and Biomaterials, China Pharmaceutical University, Nanjing 210009, China
[b] School of Chemical Engineering, Nanjing University of Science and Technology, 200 Xiao Ling Wei, Nanjing 210094, Jiangsu, China
[c] Department of Pharmaceutics, School of Pharmacy, Nanjing Medical University, Nanjing 211166, Jiangsu, China

ARTICLE INFO

Keywords:
Trident anchoring lipid
Neutrophils
Hydrophobic anchoring
Strengthened stability
Cell-based combination therapy

ABSTRACT

Anchoring-conjugation strategy, characterized by benign hydrophobic membrane anchoring and swift covalent drug-coupling, has been extensively practiced to attach therapeutic agents to cell surfaces in cell-based combination therapies. However, this approach faces significant challenges in phagocytic cells due to their enhanced membrane fluidity, which destabilizes the hydrophobic interactions and causes premature payload dissociation from cells, ultimately impairing drug delivery. This research proposes a biomimetic trident anchoring lipid featuring three hydrophobic tail chains to amplify hydrophobic interactions with the phagocyte membrane. The trident anchoring lipid thus results in robust membrane anchoring and accordingly extends drug retention on the neutrophil surface without compromising cell viability or physiological functions both in vitro and in vivo. Leveraging the inflammatory tendency of neutrophils toward the tumor vasculature, the strengthened drug conjugation facilitates effective drug delivery and site-specific release to the tumor vasculature in breast cancer models, demonstrating potent anti-angiogenic and anti-tumor efficacy. This innovative trident anchoring lipid establishes a versatile and stable drug-conjugation method for bolstering the therapeutic outcomes of neutrophil-based and potentially other cell-based combination therapies.

1. Introduction

Cell therapy serves as an emerging modality with high treatment potential in many currently intractable diseases, such as cancers, autoimmune disorders and neurodegenerative conditions [1–4]. To improve therapeutic efficacy, combination strategies involving multiple drugs have been developed in conjunction with cells, which range from direct disease treatment agents [5] to cell-boosting agents such as enhancing cellular activity [6], amplifying cellular tumor-killing capacity [7] or facilitating site-specific cell infiltration [8]. To address the challenge of inconsistent pharmacokinetics between cells and co-administered drugs to achieve the goal of efficiently collaborative treatment, living cells like neutrophils (NEs) [9], macrophage [10] et al., have been manufactured to serve as drug-delivery vehicles to achieve optimal combined effect. The common loading strategy encompasses drug-encapsulation within cells and drug-attachment on cell membrane [11]. Compared to the former, drug attachment on cell membrane is more widely employed owing to the broader applicability across both phagocytic and non-phagocytic cell types [12,13]. Moreover, it also enables spatially controlled and stimulus-responsive drug release [14]. These merits endow the strategy of drug attachment on cell membrane with superiority in forming cell-drug conjugates for future clinical application [15].

Diverse strategies have been applied on drug attachment on cell surface, mainly involving covalent binding, non-covalent attachment and gene engineering [16–18]. Of which, non-covalent drug attachment characterized by gentleness and high efficiency has been widely applied in the construction of cell-drug conjugates, such as receptor-ligand interactions [19], electrostatic adsorption [20], and anchoring-conjugation strategy [21]. Our group has developed an anchoring-conjugation strategy to anchor the liposomal avasimibe (a cholesterol esterase inhibitor) onto T cells, significantly enhancing local anti-tumor potency [21]. The anchoring-conjugation strategy utilizes favorable hydrophobic interactions between membrane-anchoring lipids and cell membranes [22], followed by stable covalent conjugation with

* Corresponding authors.
E-mail addresses: xuxiao@njust.edu.cn (X. Xu), jucaoyun@cpu.edu.cn (C. Ju), zhangcan@cpu.edu.cn (C. Zhang).

https://doi.org/10.1016/j.jconrel.2026.114903
Received 25 December 2025; Received in revised form 1 April 2026; Accepted 2 April 2026
Available online 4 April 2026

therapeutic agents, thereby achieving receptor-independent universal drug attachment. This methodology preserves membrane protein integrity while maintaining cellular functionality, demonstrating broad applicability across diverse cell types. However, the attachment stability of combined drugs on phagocytes remains challenge. Specifically, the higher membrane fluidity of phagocytes which is essential for their physiological functions like pseudopod formation and phagosome internalization [23], tends to destabilize the membrane-anchoring lipids as well as its conjugated drugs, leading to premature payload dissociation before reaching target sites. Consequently, enhancing the retention stability of therapeutic agents on cell membranes is critical for advancing the clinical efficacy of cell-based therapy based on this anchoring-conjugation strategy.

Inspired by the sperm-related glycophosphatidylinositol (GPI)-anchored decapacitation factor receptors that exhibit prolonged membrane retention due to their unique three-tailed lipid [24,25], we herein

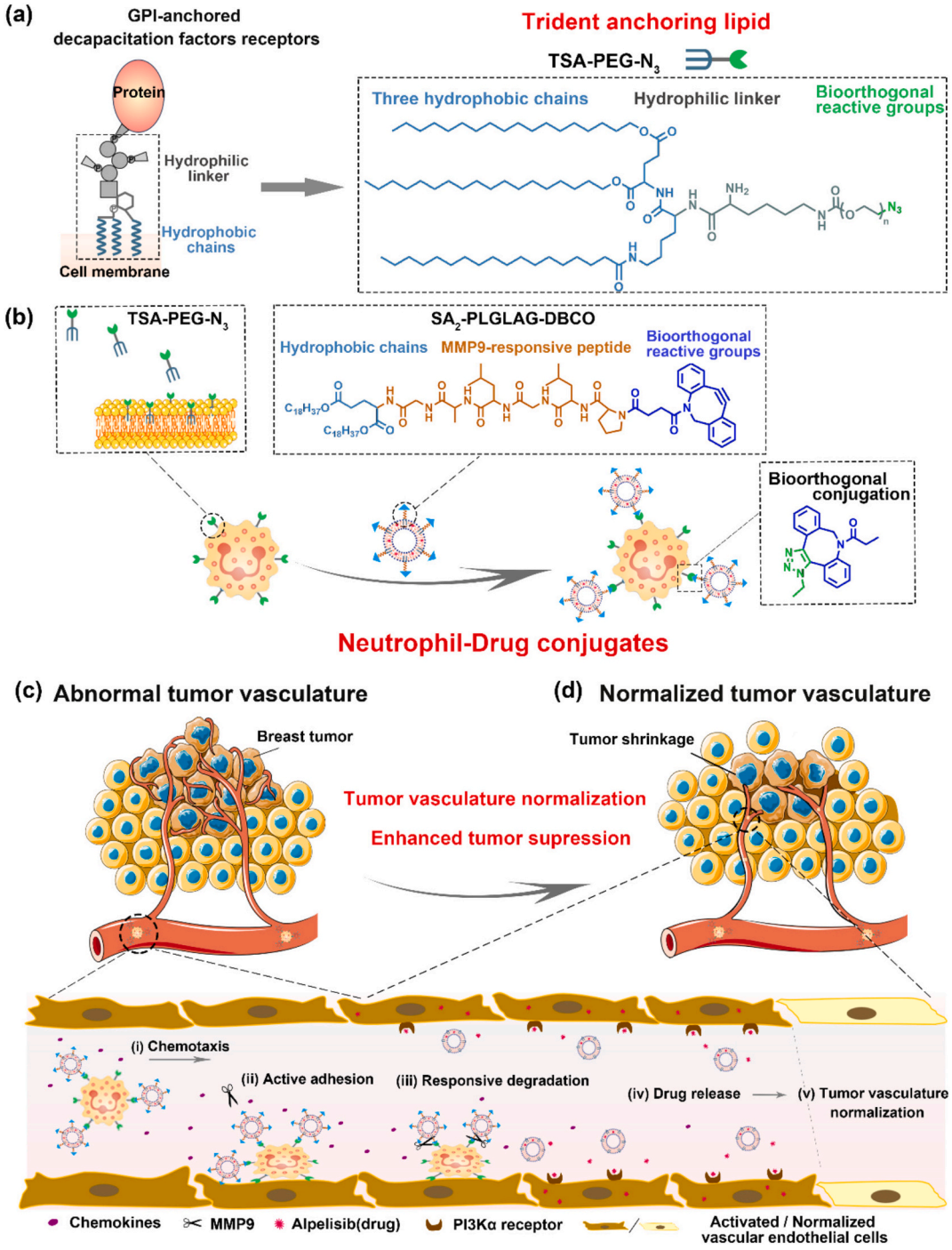

Fig. 1. Schematic illustration of NE-drug conjugates constructed by trident lipid-mediated anchoring-conjugation strategy for tumor suppression. (a) The design of biomimetic trident membrane-anchoring lipid via simulating sperm-related glycophosphatidylinositol (GPI)-anchored decapacitation factors receptors, which exhibit prolonged membrane retention on cell surface through their unique three-tailed lipid. (b) NE-Alpelisib liposome conjugates constructed by trident lipid-mediated anchoring-conjugation strategy. (c-d) Based on the inherent tumor-targeting and active adhesion of NEs on tumor vessels, NE-Alpelisib liposome conjugates with strengthened liposome-conjugation stability enabled spatial-temporal control over drug release through MMP9-mediated enzymatic cleavage, resulting in increased localized drug accumulation, thus leading to improved tumor vascular normalization as well as potentiated antitumor efficacy.

developed a series of biomimetic three-tailed membrane-anchoring lipids with adjustable hydrophilic linker lengths to reinforce the hydrophobic interactions between cells and anchored drugs, thus enhancing the drug-retained stability on cell surface (Fig. 1). Through systematic molecular dynamics simulations coupled with experimental validation, we identified an optimized trident lipid exhibiting superior membrane-anchoring stability for NEs, one of the typical phagocytes, and established a robust anchoring-conjugation method that effectively coupled liposomes onto NEs cell membranes with no influence on NEs physiological functions. Employing this trident anchoring strategy, we further constructed a matrix metalloproteinase-9 (MMP9)-responsive NE-Alpelisib liposome conjugate. This conjugate enabled the targeted release of Alpelisib at activated tumor vasculature, thereby effectively suppressing angiogenesis and improving therapeutic outcomes in breast cancer models (Fig. 1). Collectively, we established a robust NEs-based drug delivery system using a biomimetic trident anchoring strategy, improving the stability of drug attachment on cell surface. This strategy meanwhile offers broad application for other phagocytic cells-based combination therapies.

2. Materials and methods

2.1. Reagents and materials

L-Glutamic Acid was obtained from Solarbio Science & Technology Co., Ltd. (Beijing, China). p-Toluenesulfonic acid monohydrate, *N*, *N*-dimethylpyridin-4-amine (DMAP) and cholesterol were purchased from Aladdin Biochemical Technology Co.,Ltd. (Shanghai, China). Stearyl Alcohol, Stearic Acid, Boc-D-Lys-OH, Fmoc-Lys (Boc)-OH and piperidine were purchased from Bide Pharmatech Co., Ltd. (Shanghai, China). NHS-PEG-N_3 (MW = 2000, 3400, 5000 Da), DSPE-PEG2000-N_3 and mPEG2000-N_3 were purchased from Yare Biotechnology Co., Ltd. (Shanghai, China). DSPE-PEG2000-N_3-FITC, DSPE-PEG3400-N_3-FITC and DBCO-Chol were self-synthesized by our lab. DBCO-NHS was purchased from MedChemexpress LLC (USA). Fluorescein isothiocyanate (FITC) and N,N-diisopropylethylamine (DIPEA) were obtained from Energy Chemical (Shanghai, China). 1-hydroxybenzotriazole (HOBt) and 1-Ethyl-3-(3-dimethyllaminopropyl)carbodiimide hydrochloride (EDCI) were purchased from GL Biochem Ltd. (Shanghai, China), Triethylamine (Et_3N) and Trifluoroacetic acid (TFA) were purchased from Macklin Biochemical Technology Co., Ltd. (Shanghai, China). Toluene was purchased from Nanjing Chemical Reagent Co., Ltd. (Nanjing, China). Alpelisib (APLS) was purchased from MedChemexpress LLC (USA). PLGLAG was purchased from TGpeptide Biotechnology Co., Ltd. (Nanjing, China). All commercially sourced materials and reagents were used without further purification unless otherwise specified.

Soybean Lecithin was purchased from AVT Pharmaceutical Tech Co., Ltd. (Shanghai, China). Blood Cell Lysis Buffer, trypan blue, Hoechst 33342, lactate dehydrogenase test kit, reactive oxygen species test kit and TNFα were purchased from Beyotime Biotechnology Co., Ltd. (Shanghai, China). Percoll was purchased from GE Healthcare Co., Ltd. (Chicago, IL, USA). Annexin V-PE/7ADD Apoptosis Detection Kit was purchased from Vazyme Biotechnology Co., Ltd. (Nanjing, China). DiR was purchased from KeyGen Biotech (Nanjing, China). Rhodamine-DHPE and Alexa Fluor™ 488 CD162 (PSGL-1) Monoclonal Antibody were purchased from Thermo Fisher Scientific (USA). PE anti-mouse CD182 (CXCR2) Antibody, FITC anti-mouse CD11b Antibody, APC anti-mouse CD62L Antibody, Alexa Fluor 594 anti-CD31 antibody and FITC anti-mouse CD106 were purchased from Biolegend (San Diego, CA, USA). N-Formyl-Met-Leu-Phe (fMLP) was purchased from Sigma-Aldrich® (MA, USA). Membrane fluidity test kit was purchased from Abcam (Cambridge, UK). Phorbol 12-myristate 13-acetate (PMA) was purchased from MedChemExpress (USA). FITC-phalloidin was purchased from ABclonal (Wuhan, China). Matrix metalloproteinase 9 (MMP9) was purchased from Absin Bioscience Inc. (Shanghai, China). Mouse MMP9 ELISA Kit was purchased from Elabscience Biotechnology Co., Ltd. (Wuhan, China). CFDA-SE Cell Proliferation and Tracking Detection Kit was purchased from Beyotime (Shanghai, China). BD Matrigel was purchased from BD Biosciences (USA). D-Luciferin Potassium Salt was purchased from Yeasen Biotechnology Co., Ltd. (Shanghai, China). *Lycopersicon esculentum* (Tomato) Lectin (LEL, TL) DyLight 649 was purchased from Thermo Fisher Scientific (USA).

2.2. Cell lines and animals

NEs were isolated from mouse bone marrow according to our previous reported methods [8]. HUVEC cell lines were cultured in DMEM medium containing 10% FBS. 4T1 and 4T1-luciferase tumor cells were cultured in RPMI 1640 medium containing 10% FBS. SVEC4–10 were purchased from Pricella Biotechnology Co., Ltd. (Wuhan, China) and cultured in DMEM medium containing 10% FBS. All cells were cultured in medium containing 1% penicillin-streptomycin in a humidified incubator at 37 °C with 5% CO_2.

BALB/c mice (females, 6–8 weeks, 18–20 g) were purchased from the Zhejiang academy of medical sciences. All animals were pathogen free and allowed access to food and water freely. All procedures were approved by the Animal Ethics Committee of China Pharmaceutical University and were conducted in compliance with the Guide for Care and Use of Laboratory Animals.

2.3. Instrument for compound analysis

The detailed synthesis process was provided in the supporting information. All ^1H NMR and ^{13}C NMR spectra were recorded on Bruke AVANCE III HD 300 MHz and 600 MHz spectrometers and the spectra were processed and analyzed using MestReNova software. HRMS was recorded on Agilent Technologies 6200 series TOF/6500 series Q-TOF. The FTIR spectra were recorded by Bruker Tensor 27. The MALDI-TOF-MS analysis was performed on a Bruker UltrafleXtreme MALDI-TOF/TOF mass spectrometer operated in reflector mode. The instrument was equipped with a 355 nm Nd:YAG laser and positive ion TOF detection, using an accelerating voltage of 20 kV. The laser focus voltage was set to 8.02 kV, and the pulsed ion extraction time was optimized to 170 ns. Data acquisition and analysis were controlled by FlexControl 3.4 and FlexAnalysis 3.4 software, respectively. The matrix solution was prepared by dissolving 2,5-dihydroxybenzoic acid (DHB) in chloroform (15 mg/mL). External calibration was performed using a standard solution prior to each experiment.

2.4. Optimizing the membrane anchoring of TSA-PEG-N_3-FITC

To evaluate the effect of TSA-PEG-N_3-FITC concentration on membrane-anchoring, the fresh isolated NEs (2×10^6) were incubated with TSA-PEG-N_3-FITC (PEG MW = 2000, 3400, 5000 Da) under a series of concentrations for 10 min in the specific RPMI 1640 medium containing 15% PEG400 (*v*/v). The optimal anchoring concentration was determined according to better cell viability (>80%) and minimum uptake by confocal microscope (LSM 800, Carl Zeiss Inc.) and flow cytometry (Attune NXT, Thermo Fisher Scientific).

2.5. Cell viability

The NEs viability after anchoring or liposome conjugation were evaluated by the Annexin V-PE/7ADD apoptosis detection kit in flow cytometry (Attune NXT, Thermo Fisher Scientific).

2.6. Measurement of critical micelle concentration

The critical micelle concentration (CMC) of anchoring molecules was detected by pyrene fluorescence assay. Specifically, 100 μL of pyrene acetone solution (25 μg/mL) was aliquoted into 5 mL centrifuge tubes and allowed to evaporate overnight at room temperature. Subsequently,

the aqueous solutions containing TSA-PEG-N_3 (MW = 2000, 3400, 5000 Da) or DSPE-PEG2000-N_3 were added to the pyrene-coated tubes. The mixtures were incubated at 60 °C for 1 h with gentle agitation, followed by 2 h ultrasonication and 12 h equilibration in darkness. The emission spectrum of pyrene was detected by fluorescence spectrophotometer (Cary Eclipse, Agilent) with the excitation wavelength at 372 nm. The I1/I3 intensity ratio of pyrene's first (374 nm) and third (386 nm) emission peaks exhibited concentration-dependent changes. The CMC corresponded to the median value of the abrupt change in the I1/I3 curve with concentration.

2.7. Measurement of water contact angle

The static water contact angle (WCA) of TSA-PEG and DSPE-PEG was evaluated on spin-coated thin films. Briefly, each lipid-PEG conjugate was dissolved in chloroform at a concentration of 1 mg/mL, then spin-coated onto a clean polished silicon wafer to form a uniform thin film. The films were subsequently placed under vacuum for 2 h to ensure removal of organic solvent. WCA measurements were performed at a standard contact angle goniometer using ultrapure water. The profile of the water droplet was captured immediately after deposition, and the contact angle was determined from the captured image using the Young-Laplace fitting method.

2.8. Quantification of fluorescence distribution on cell membrane and cytoplasm

The trypan blue (TB) solution was used for quantifying the distribution of anchoring molecules on NEs membrane and cytoplasm. The proportion on membrane and in cytoplasm was respectively calculated by the following Eqs. (1)–(2):

$$\text{Ratio on membrane}\ (\%) = \left(\text{MFI}_{\text{before}} - \text{MFI}_{\text{after}}\right)/\text{MFI}_{\text{before}} \times 100\% \quad (1)$$

$$\text{Ratio in cytoplasm}\ (\%) = \text{MFI}_{\text{after}}/\text{MFI}_{\text{before}} \times 100\% \quad (2)$$

Here $\text{MFI}_{\text{before}}$ and $\text{MFI}_{\text{after}}$ represented the mean fluorescence intensity (MFI) of NEs (10,000 events) by flow cytometry (Attune NXT, Thermo Fisher Scientific) before and after TB quenching.

The anchoring amount on membrane was obtained from the difference in fluorescence intensity between the initial total anchoring molecules and incubation supernatant after membrane anchoring, which were respectively measured at excitation and emission wavelengths of 495 nm and 520 nm by microplate reader (BioTek, Agilent). The fluorescence intensity was converted into the amount (mol) of anchoring molecules through the standard curve of fluorescence intensity-concentration (mol/L). The anchoring amount on NEs was calculated by the following Eq. (3):

$$\text{Anchoring amount} = (m_i - m_s) \times \text{Ratio on membrane}\ (\%) \quad (3)$$

Here m_i and m_s respectively represents the quantity (mol) of the initial anchoring molecules and the incubation supernatant.

2.9. Molecular dynamics simulation

The GROMACS 2022.1 simulation software package [26] was employed for the simulations. For the initial configuration of the simulation system, the lipid membrane is preassembled into a 20 × 20 nm^2 layer including more than 400 POPC/CHOL/DPSM molecules by the CHARMM-GUI Martini maker tool and positioned at the center of the simulation box. Three-dimensional periodic boundary conditions were used for the simulation box. The system is solvated by standard Martini water and symmetric NaCl solution at the concentration of $c_s = 150$ mM to model physiological conditions. Energy minimization was performed using the steepest descent algorithm without any constraints, followed by conical NVT and NPT equilibration simulations for 10 ns at a temperature of 310 K for each group using the velocity rescale temperature coupling scheme.

To compute the binding free energy between an anchoring-molecule and the membrane bilayer, the Steered Langevin Dynamics (SLD) simulation was employed to compute the potential of mean force (PMF) of the lipid with the "pull code" as implemented in the GROMACS software package. The anchoring-molecule was initially placed away from the membrane surface. In each run, an external harmonic potential was launched to the molecule, which moved with a constant pulling velocity v_p in order to steer the molecule toward the membrane. The reaction coordinate r was selected as the distance between the terminal bead of a given anchoring-molecule in its hydrophobic tail and the center of mass (COM) of the membrane along the z axis, where z pointed out the direction perpendicular to the membrane surface. To ensure adequate sampling, the pull rate was chosen small as $v_p = 0.001$ nm ns^{-1} and a harmonic force constant of K = 2500 kJ mol^{-2} was used.

2.10. Quartz crystal microbalance with dissipation (QCM-D) analysis

The interfacial interactions of anchoring molecules with a model lipid bilayer and their insertion stability were quantitatively evaluated by QCM-D (Q-Sense Explorer, Biolin Scientific, Sweden). A supported lipid bilayer (SLB) was formed on silica-coated quartz sensor crystals. After stabilizing the baseline with PBS buffer at a flow rate of 40 μL/min, an SLB composed of DOPC, SM and chol (1: 1: 1, molar ratio) was formed via the vesicle fusion method. The chamber was then rinsed extensively with PBS to remove any unfused vesicles. Following SLB stabilization, a solution of anchoring molecules (l μM in PBS) was injected at 40 μL/min. The adsorption process was monitored until the frequency shift (Δf) reached a plateau, and subsequently preformed PBS rinsing for at least 30 min to remove weakly associated molecules. The entire adsorption-rinsing cycle was simultaneously tracked by recording the changes in resonance frequency (Δf) and energy dissipation (ΔD) of the quartz crystal.

2.11. Liposomal APLS conjugation on anchored NEs

The MMP9-responsive Alpelisib (APLS) liposomes was prepared by 50 mg SPC, 8 mg Chol, 8 mg DBCO-PLGLAG-SA_2 and 2.2 mg APLS. For fluorescence label, Rhodamine B-DHPE (2.5 mg/mL in methanol, 100 μL) was added. All components were dissolved in 1 mL ethanol, and slowly dripped at 1 mL/min into 3 mL ultrapure water preheated to 60 °C, followed by stirring at 900 rpm/min for 2 h to evaporate the organic solvent. Then the solution was sonicated (30% power) for 15 min in ice bath and filtered through a 0.45 μm microporous filter membrane to obtain APLS liposomes. The zeta-potential and particle size were detected by NanoBrook Omni (Brookhaven) and Transmission electron microscope.

Anchored NEs (2×10^6) incubated with diluted APLS liposomes in RPMI 1640 medium for 30 mins at 37 °C. The recovered Lipo/APLS@NEs were detected by the confocal microscope (LSM 800, Carl Zeiss) and flow cytometry (Thermo Attune NXT). To quantify the APLS loading amount, Lipo/APLS@NEs were resuspended in 100 μL of RIPA lysis buffer for 30 mins to achieve complete cell lysis. Subsequently, 900 μL of methanol was added to extract drug for 30 min. The mixture was then vortexed vigorously for 3 min and centrifuged at 12,000 rpm for 10 min. The resulting supernatant was collected and subjected to HPLC analysis to determine the drug content.

2.12. Stability of lipid anchoring or liposomal APLS conjugation on NEs in different physiological conditions

Anchored NEs or liposomes (labeled by rhodamine B) conjugated NEs were respectively settled in RPMI 1640 medium with 10% FBS or

10 nM fMLP for 8 h. The released anchoring molecules or drugs in recovered supernatant was quantified by microplate reader and HPLC. The remained anchoring molecules or drugs on NEs were detected by flow cytometry and HPLC. The fluorescence was converted to the molar amount on membrane by trypan blue quenching as mentioned above.

The distribution of anchoring molecules during the transvascular migration was evaluated in the transwell chamber (polycarbonate membrane: 3 μm pore size, 12 mm diameter and 1.12 cm^2 membrane surface area, Corning). The blood vessel model was established with HUVEC cell monolayer in transwell. HUVEC (1×10^5 cells) were seeded into the upper chamber of transwell, and cultured for 4–7 days until the transepithelial electrical resistance (TEER) above 300 Ω·cm^2 measured by Millicell-ERS voltohmmeter (Millipore Corporation, Millicell® ERS-2, MA, USA). Anchored NEs (1×10^6 cells) were added into the upper chamber, and RPMI 1640 containing 10% FBS (v/v) with 10 nM fMLP were added in the lower chamber. After 8 h of incubation, recovering the cells in the lower chamber and the HUVEC monolayer to detect the fluorescence intensity using microplate reader (BioTek, Agilent).

2.13. Parallel-plate flow chamber assay

The stability of the membrane-anchoring or liposome-conjugation on NEs under the shear stress from blood flow were evaluated using parallel-plate flow chamber (Glycotech). According to the gasket size of the parallel plate flow chamber (0.25 cm wide, 0.01 in thick), the membrane-anchored or liposome-conjugated NEs (2×10^6 cells, 50 μL) were seeded in the same size area on 3.5 cm dish (Corning) pre-coated by poly-L-lysine solution (0.1 mg/mL) to keep complete adhesion. Under the vacuum condition, the flow rate set at 0.42, 1.2, 2.1 mL/min could generate the corresponding shear force of 2, 6 and 10 dyn/cm^2 for the adherent NEs. After continued flowing for 5 min, the flowed buffer was recovered. The released anchoring molecules or drugs was detected after buffer freeze-drying. The retained amount on NEs were determined by subtracting the released.

2.14. Basic physiological functions of NEs

The membrane-anchored and liposome-conjugated NEs were immediately tested after preparation. Blank NEs without any treatment were used as control. The cell membrane permeability and fluidity of NEs were detected respectively by LDH test kit and membrane fluidity test kit. The expression of critical membrane markers CD11b, CXCR2, CD62L and PSGL-1 were detected by flow cytometry. The chemotaxis capacity of NEs were investigated using transwell chamber. NEs (1×10^6 cells) were added into the upper chamber, and RPMI 1640 containing 10% FBS (v/v) with 10 nM fMLP were in the lower chamber. The number of NEs in the lower chamber through chemotaxis (after 3 h of incubation) was photographed randomly and counted by Image J. The chemotaxis index was calculated from the following Eq. (4):

$$\text{Chemotaxis index} = (N - N_{control})/N_{control} \quad (4)$$

N was the counted numbers of liposome-conjugated NEs in the lower chamber in the presence of fMLP, and $N_{control}$ was the number of blank NEs in the lower chamber without fMLP.

Blank NEs and liposome-conjugated NEs were seeded on confocal dish pre-coated by poly-L-lysine solution (0.1 mg/mL). The NEs were stimulation by 100 nM fMLP for 15 min to make cells polarized and fixed by 4% PFA for 10 min. After rinsing, the cell cytoskeletal F-actin protein was labeled by the FITC-phalloidin (1:100) with 0.1% Triton X-100 for 30 min in room temperature. The cell polarization was observed by the confocal microscope (LSM 800, Carl Zeis s Inc.)

2.15. Glycolysis stress test

Blank NEs and liposome-conjugated NEs were resuspended in XF assay media at a concentration of 5×10^5/mL onto a XF96 cell plate pre-coated with poly-L-pysine (0.1 mg/mL). Before test, the medium was removed from the cell plate and the cells were washed three times with Seahorse XF base medium with 3 mM L-glutamine and incubated for 45 min at 37 °C. Afterwards glycolysis stress test was performed in the Seahorse XFe96 analyzer (Agilent) according to the protocol provided by the manufacturer. The extracellular acidification rate (ECAR) of NEs was measured in real-time by subsequently injection of 10 mM glucose, 2 μM oligomycin and 50 mM 2-deoxyglucose. Measurements were done in at least 12 replicates per plate.

2.16. Biodistribution and specific APLS release of Lipo/APLS@NEs

The APLS liposomes were settled respectively in the 1640 medium containing 10% FBS with 20 nM MMP9 or not. The particle size was detected by NanoBrook Omni (Brookhaven) and the morphology change was observed by TEM. The APLS release was quantified by HPLC (LC-2010AHT, Shimadzu) as mentioned above. Lipo/APLS@NEs were also set in RPMI 1640 medium containing 10% FBS with 20 nM MMP9 or not. The released and retained APLS on NEs was quantified by HPLC.

4 T1 tumor cells were inoculated in situ on BALB/c mice, and tumor-bearing mice were divided into three groups ($n = 3$ mice per group). Different reagent or formulations including DiR (1 mg/kg), DiR-labeled NEs (2×10^7) and DiR-labeled Lipo/APLS@NEs (2×10^7) were respectively intravenously administrated. At various time points post-injection (2, 6, 12, 24, 48 h), tumors and organs were excised for fluorescence imaging analysis for the NEs biodistribution using IVIS Spectrum system (PerkinElmer).

Furthermore, for investigating the APLS distribution in vivo, Lipo/APLS (80 μg of APLS each mouse) and Lipo/APLS@NEs (2×10^7, equivalent to 80 μg of APLS) were respectively intravenously administrated ($n = 3$ mice per group). At the same time points post-injection, tumors and organs were harvested and weighed. Tissue samples were processed by dispersion homogenization in saline and subjected to protein precipitation with methanol. After centrifugation at 12000 rpm for 10 mins, supernatants were collected for HPLC analysis of APLS concentration.

The in vivo drug release in the tumor blood vessel was evaluated. The responsive Lipo/APLS@NEs and non-responsive Lipo-APLS@NEs (2×10^7) were infused into tumor-bearing mice intravenously, for which Lipo-APLS were labeled by Rho B and NEs were labeled by AF488 anti-mouse Ly6G. The tumor tissues were collected in different time after injection and prepared into frozen sections. The tumor vessels were labeled by Tomato Lectin DyLight 649 and observed the real-time distribution of NEs and APLS liposomes by the confocal microscope (LSM, Carl Zeiss).

2.17. In vitro anti-angiogenesis effect of Lipo/APLS@NEs

The proliferation inhibition of blood vessel endothelial cells was evaluated by pre-stimulating SVEC4–10 cells with 50 ng/mL TNFα in DMEM medium containing 10% FBS for 4 h. The activated SVEC4–10 cells were confirmed via the expression of VCAM-1 and the release of MMP9. Then activated SVEC4–10 cells were labeled with 1 mL CFDA-SE for 10 mins. After PBS washing, SVEC4–10 cells (5×10^4) were added in the lower chamber of the transwell chamber (24 wells, 0.4 μm), then different formulations were added on the upper chamber: 1) DMEM complete medium; 2) 5×10^5/mL NEs; 3) 2 μg/mL APLS; 4) 5×10^5/mL Lipo/APLS@NEs; 5) 20 nM MMP9; 6) 20 nM MMP9 and 5×10^5/mL NEs; 7) 20 nM MMP9 and 2 μg/ mL APLS; 8) 20 nM MMP9 and 5×10^5/mL Lipo/APLS@NEs. After incubation for 48 h, the SVEC4–10 cells were recovered from the lower chamber and detected from the flow cytometry (Thermo Attune NXT).

The invasion inhibition was evaluated by seeding activated SVEC4–10 cells in 24-wells plate and a uniformity scratch was made to the cell monolayer. Transwell chamber was also used here and same formulations mentioned above were respectively added to the upper

chamber. The scratches at the same position in the lower chamber were observed and photographed by microscope at 0 h and 12 h. The scratch recovery rate for evluating the invasion of endothelial cells was calculated with the formula (5):

$$\text{Scratch recovery rate} = \left(A_{initial} - A_{final}\right)/A_{initial} \quad (5)$$

Where $A_{initial}$ and A_{final} respectively meant the initial and final scratch area as measured by Image J.

To evaluate the effect of Lipo/APLS@NEs on the tube formation ability, a 24-well plate was coated with 200 μL of Matrigel at 37 °C for 30 min to allow complete gel polymerization. Activated SVEC4–10 cells (1.25×10^5 cells/mL, 200 μL) in DMEM medium with 10% FBS were carefully added onto the solidified Matrigel, avoiding contact with the gel surface to prevent scratches or damage. Afterwards, transwell chamber were used here and same formulations mentioned above were respectively added to the upper chamber for incubation of 6 h. Tube formation was observed and imaged. The tube length and branching points were measured using Image J.

2.18. Therapeutic efficacy and biosafety evaluation of NEs-APLS liposome conjugates for triple-negative breast cancer

4 T1 or 4 T1-luc tumor cells (1×10^6 cells) were inoculated in situ on BALB/c mice, and tumor-bearing mice were randomized into six groups on day 7 post-inoculation ($n = 5$ mice per group). Different formulations were administered intravenously on days 7, 11, 15, and 19 post-inoculation: 1) Saline; 2) NEs (2×10^7 cells); 3) Lipo/APLS (4 mg/kg) + NEs (2×10^7 cells); 4) Lipo-APLS@NEs (2×10^7 cells); 5) Lipo/APLS@NEs (2×10^7 cells). Free APLS (20 mg/kg) was administered by daily gavage from days 7–21 after tumor inoculation. Tumor growth was monitored via bioluminescence imaging (AniView, Biolight Biotechnology Co., Ltd). Tumor volume was measured by vernier caliper and calculated with the formula (6):

$$V = \left(L \times W^2\right)/2 \quad (6)$$

where L meant the longest axis and W meant the shortest axis of tumor. Mice were euthanized on day 21 for tumor excision and weighing. Tumor angiogenesis was quantified via $CD31^+$ microvessel density measurements in Alexa Fluor 594-immunostained tumor sections. Based on the dosing regimen above, the survival status of mice was recorded daily from the day of tumor inoculation ($n = 5$ mice per group). Mice were euthanized if tumor volume exceeded 1500 mm^3.

The biosafety evaluation was conducted based on the dosing regimen above ($n = 3$ mice per group). Body weights of mice in each group were meticulously recorded on days 7, 9, 11, 13, 15, 17, 19, and 21 post-tumor inoculation. These measurements were used to construct body weight-time curves, enabling a detailed comparison of body weight changes across different experimental groups. On day 21 post-inoculation, the organs of mice were harvested including heart, liver, spleen, lung, and kidney tissues. Organ-to-body weight ratios were calculated to evaluate potential organ-specific effects. The harvested organs were processed for paraffin embedding, sectioned, and stained with hematoxylin and eosin (H&E) for histopathological examination, allowing for the assessment of any structural alterations or damage. Additionally, blood samples were collected from the mice via retro-orbital puncture for the isolation of serum on day 21 post-inoculation. Levels of hepatic markers aspartate transaminase (AST) and alanine aminotransferase (ALT), as well as renal markers urea nitrogen (BUN) and creatinine (CRE), were quantified in the serum samples using standard biochemical assays.

2.19. The effect of drug-conjugation stability on anti-tumor therapy in vivo

To further evaluate the anti-tumor efficacy influenced by the stability of liposome conjugation, NEs-liposome conjugates were prepared respectively by TSA-PEG3400-N_3 or DSPE-PEG2000-N_3 anchoring. Lipo/APLS@NEs mediated by TSA-PEG3400-N_3 or DSPE-PEG2000-N_3 anchoring respectively (equivalent to 80 μg APLS per mouse) were intravenously injected into tumor-bearing BALB/c mice. At 2, 6, 12, 24 and 48 h post-injection ($n = 3$ mice per group), collected tumor tissues were processed as mentioned above. The supernatant was collected for HPLC analysis of APLS concentration.

The varying stabilities of liposome conjugations were anticipated to result in distinct anti-tumor efficacies. Saline, Lipo/APLS@NEs (TSA-PEG3400-N_3 anchoring) and Lipo/APLS@NEs (DSPE-PEG2000-N_3 anchoring) (equivalent to 80 μg of APLS each mouse) were administered intravenously on days 7, 11, 15, and 19 post-tumor inoculation ($n = 5$ mice per group). The tumor growth, tumor volume and tumor weight were measured as described above. The tumor prolification was also evaluated by Ki67 immunohistochemical staining of tumor sections after mice were euthanized on day 21. Tumor angiogenesis was quantified via $CD31^+$ microvessel density measurements in Alexa Fluor 594-immunostained tumor sections. Based on the dosing regimen above, the survival status of mice was recorded daily from the day of tumor inoculation (n = 5 mice per group) and mice were euthanized if tumor volume exceeded 1500 mm^3.

2.20. Statistics

Statistical analysis was performed using the GraphPad Prism 8.0 software. All graphical data were presented as mean ± SD in at least triplicate. Statistical significance was determined using two-tailed unpaired Student's *t*-test, One-way ANOVA and Two-way ANOVA, in which $P < 0.05$ were considered statistically significance. A log-rank (Mantel-Cox) test was used to analyze the statistical significance in the survival analysis.

3. Results

3.1. Design and synthesis of bioinspired trident membrane-anchoring lipids to potentiate the hydrophobic interaction with NEs membrane

As reported, the natural phospholipid conjugated to polyethylene glycol (PEG), such as DSPE-PEG, has been widely applied in cell membrane anchoring including NEs [8,21]. In our previous research, NEs were preloaded with nanodrugs to partially saturate the phagocytosis before DSPE-PEG2000 anchoring, thus reducing the cellular uptake and increasing the anchoring efficiency. To evaluate the feasibility of direct anchoring on NEs, the FITC-labeled DSPE-PEG2000-N_3 (DSPE-PEG2000-N_3-FITC) was applied as the fluorescent anchors, which showed satisfying anchoring effect on NEs. Notably, we found DSPE-PEG2000-N_3-FITC gradually shed from the NEs membrane with approximately 52% remaining membrane-anchored after 8 h (Supporting Information Fig. S1), consistent with the previously reported membrane kinetics of drug-preloaded NEs [8]. We speculated that this detachment mainly stemmed from insufficient interaction strength between the double-tailed lipid and the cell membrane [27], which crucially existed as a universal issue for hydrophobic interaction-based cell membrane anchoring [28,29].

To address this limitation, we designed a novel trident membrane anchor, TSA-PEG, inspired by the stable membrane association of sperm-related GPI-anchored decapacitation factor receptor, which features three hydrophobic tails [24,25]. TSA-PEG incorporates three octadecyl chains and a variable-length PEG linker, extending from the conventional double-tailed DSPE-PEG structure (Fig. 2A). To theoretically predict the anchoring stability of TSA-PEG versus DSPE-PEG, molecular dynamics (MD) simulation was performed based on coarse-grained models on a model NE membrane which contained three recognized components of phosphatidylcholine (POPC), sphingomyelin (SM) and cholesterol (Chol) [30] (Fig. 2A and B). The pulling simulation

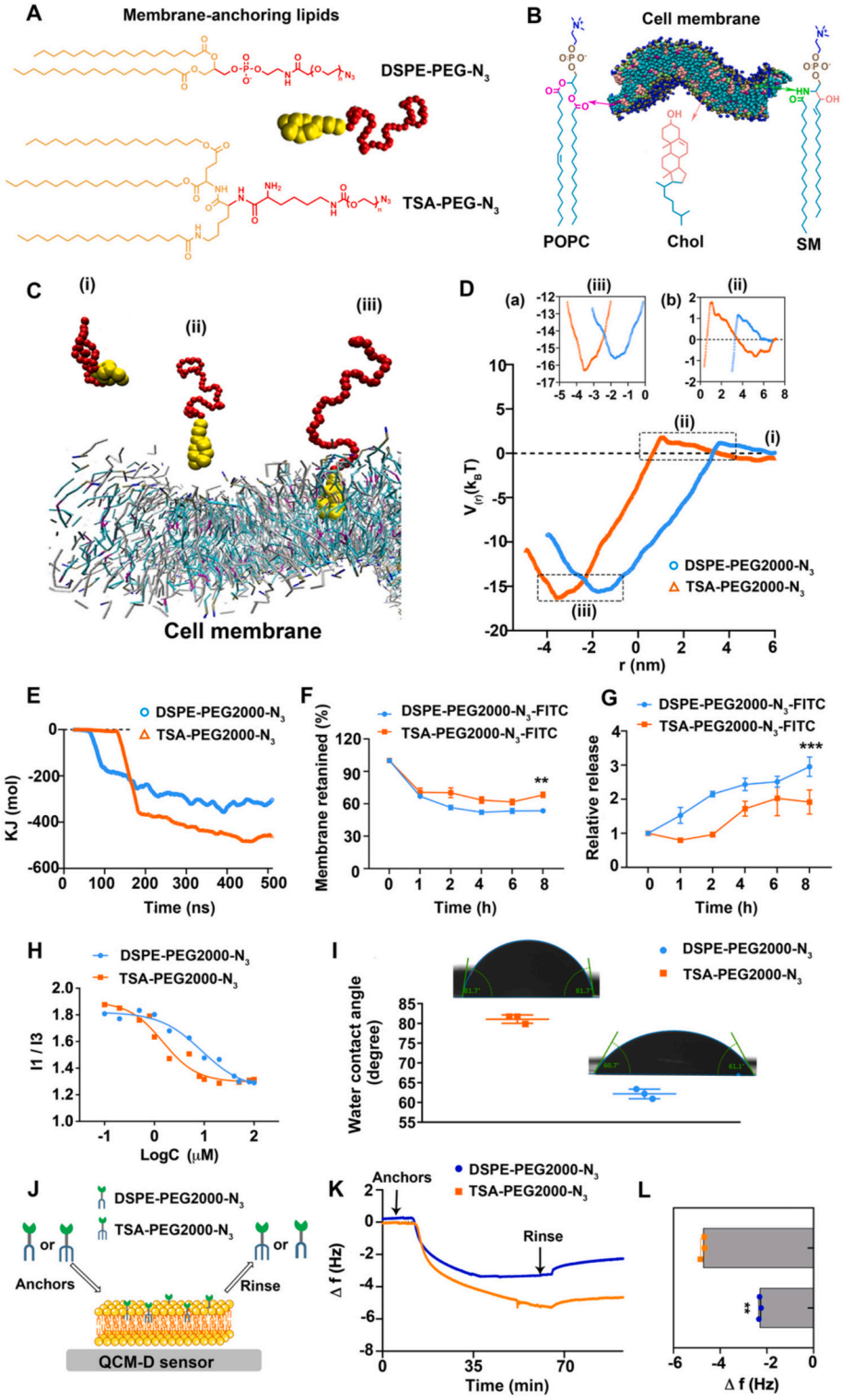

Fig. 2. Design and synthesis of bioinspired trident membrane-anchoring lipids to potentiate the hydrophobic interaction with NE membrane (A) The coarse-grained Martini models of membrane-anchoring lipids with two- or three-tailed hydrophobic chains. (B) The coarse-grained Martini models of cell membrane simulated by three representative lipid components of POPC, SM and Chol. (C) Membrane-anchoring process: (i) unbound state where the lipid tails (yellow) are not extended; (ii) initial anchoring when lipid tails (yellow) are extended; (iii) the complete insertion state into the membrane layer. (D) The potential of mean force (PMF) V(r) calculated between anchoring lipid and membrane as a function of the reaction coordinate r. The V(r) of state (iii) and state (ii) were respectively showed in the enlarged view (a) and (b). (E) The Lennard-Jones short-range binding energies obtained from molecular dynamics simulation between TSA-PEG2000-N_3 and the membrane layer, and between DSPE-PEG2000-N_3 and the membrane layer. (F-G) The anchoring stability of DSPE-PEG2000-N_3-FITC and TSA-PEG2000-N_3-FITC, including the proportion of anchoring lipid retained on NE membrane (F) and the fluorescence quantity in the culture supernatant with time (G). Data are mean ± SD ($n = 3$). (H) The critical micelle concentration of TSA-PEG2000-N_3 and DSPE-PEG2000-N_3. (I) The water contact angle of TSA-PEG2000-N_3 and DSPE-PEG2000-N_3. Data are mean ± SD (n = 3). (J-L). (For interpretation of the references to colour in this figure legend, the reader is referred to the web version of this article.)

calculated the potential of mean force profile $V(r)$ of the anchors in relation to the center of mass (COM) distance r between the lipid and the membrane center. The key distances corresponding to $V(r) = 0$, maximal $V(r)$, and minimal $V(r)$ indicated a three-phase membrane insertion process for the anchoring lipids: (i) unanchored state, (ii) initial anchoring, and (iii) anchoring completion (Fig. 2C). At the anchoring process, we observed a notable feature of TSA lipid that a sudden increase in $V(r)$ just above 0 (Fig. 2D (b)), marking the onset of anchoring. This energy barrier represented the energy penalty associated with initiating lipid anchoring. Specifically, we observed significant stretching of the lipid as it contacted the membrane, which rapidly elongated the lipid tail to reach the membrane's hydrophobic layer. This mechanism offset the energy penalty for lipid insertion and considerably reduced the energy barrier for initiating the anchoring process. Moreover, despite TSA-PEG held a much larger lipid tail comprised of three chains than DSPE-PEG with two chains, the height of the energy barrier V(r) was also small, measuring 1.77 k_BT for TSA-PEG (Fig. 2D (b)), suggesting the easy insertion of TSA lipid. After anchoring completion, the membrane-lipid binding free energy ΔG was determined as the minimum of $V(r)$, yielding values of −16.4 k_BT for TSA-PEG and − 15.6 k_BT for DSPE-PEG (Fig. 2D (a)). Since energy minimization corresponded to greater system stability, this demonstrated that TSA-PEG anchoring conferred greater stability compared to DSPE-PEG at the same PEG linker length. Moreover, the time required for the lipid to transition from a bound to an unbound state was approximately 2.2 times longer for TSA-PEG than DSPE-PEG in the context of Kramers' theory, further indicating that lipid TSA-PEG demonstrated more delayed shedding and improved stability. In addition, the binding energy between the anchoring molecules and cell membrane directly reflected the binding strength. The sharp decrease in E_{LJ} signified the establishment of hydrophobic interaction with cell membrane. The lower energy minimum of TSA-PEG indicated stronger binding strength with membrane over DSPE-PEG (Fig. 2E), which accounted for the greater anchoring stability of TSA-PEG.

Subsequently, azide-functionalized TSA-PEG2000 (TSA-PEG2000-N_3) was synthesized for anchoring-conjugation (Supporting Information Scheme S1). All intermediates and the final product were characterized by ^{1}H NMR, ^{13}C NMR, mass spectrometry (MS), and fourier transform infrared spectroscopy (FTIR) (Supporting Information Fig. S2-S10). Its FITC-labeled derivative (TSA-PEG2000-N_3-FITC) was applied for convenient observation. Experimentally, the membrane-binding stability of TSA-PEG2000-N_3-FITC was significantly superior to that of DSPE-PEG2000-N_3-FITC, as evidenced by its slower release kinetics and higher retention rate. Over 8 h, TSA-PEG2000-N_3-FITC demonstrated a 1.3-fold higher membrane retention rate (70% vs. 54% at 8 h; Fig. 2F). Consistently, the shedding of DSPE-PEG2000-N_3-FITC was 1.5-fold greater than that of TSA-PEG2000-N_3-FITC (Fig. 2G). We attributed the strengthened membrane-binding of TSA-PEG primarily to the increased hydrophobicity of TSA anchor, which was then verified by pyrene-based CMC measurement and water contact angle measurement. Specifically, we detected a substantially lower CMC for TSA-PEG2000-N_3 (1.48 μM) than for DSPE-PEG2000-N_3 (8.85 μM) in water, and a 20-degree increase for the TSA anchor over the DSPE anchor in water contact angle, which overall confirmed the higher hydrophobicity of TSA-PEG2000-N_3 (Fig. 2H, I, Supporting Information Table S1), implying the potentiated interaction with the cell membrane of NEs. Then we directly evaluated the interfacial interaction of different anchors with lipid bilayer membrane using Quartz Crystal Microbalance with Dissipation (QCM-D) (Fig. 2J, Supporting Information Fig. S17A), which revealed strong adsorption of both TSA-PEG2000-N_3 and DSPE-PEG2000-N_3 onto the supported lipid bilayer, as reflected by substantial negative frequency shifts (Δf) and concurrent positive dissipation shifts (ΔD). Upon rinsing, the increased Δf for both systems indicated mass removal, while the ΔD remained largely unchanged at a positive value (Fig. 2K and Supporting Information Fig. S17B). This suggested that rinsing selectively removed weakly associated molecules, leading to a rigid coupled structure, thus supporting the formation of stable lipid insertion into the bilayer. In contrast, mPEG2000-N_3 (lacking a lipid moiety) exhibited rapid adsorption and synchronized reversal of both Δf and ΔD to baseline upon rinsing (Supporting Information Fig. S17C), indicating a pure surface adsorption without stable lipid integration. Notably, after rinsing, the Δf of TSA-PEG2000-N_3 remained significantly lower than DSPE-PEG2000-N_3 (Fig. 2L), suggesting a greater amount of TSA-PEG2000-N_3 was stably incorporated into the membrane following the removal of weakly adsorbed part. We therefore attributed the superior retention of TSA-PEG2000-N_3 was consistent with its higher hydrophobicity, which facilitated more stable integration into the lipid membrane.

Collectively, these results demonstrated that augmenting the hydrophobicity of the anchor, exemplified by increasing the number of hydrophobic tails from two to three, was a viable strategy to strengthen membrane binding and minimize anchors detachment.

The adsorption and insertion of different anchors on a lipid bilayer membrane were evaluated by QCM-D (J), as represented by the changes in frequency (K). The Δf values was obtained by initial measurements (t = 0 min) and final measurements after buffer rinse (L). Data are mean ± SD (n = 3 replicate experiments). $^{**}P < 0.01$ and $^{***}P < 0.001$ by Two-way ANOVA in (F, G) and Student's t-test in (L).

3.2. Influence of hydrophilic group of trident membrane-anchoring lipid on the anchoring efficiency and stability of NEs

As reported, anchoring molecules with different PEG molecular weight has showed different anchoring behavior [27]. Since the impact of lipid structures on anchoring stability of lipid-PEG was evaluated, we next aimed to investigate how the hydrophilic group, such as the PEG molecular weight (2000, 3400, 5000 Da), affected membrane insertion. To this end, we further synthesized azide-functionalized TSA-PEG3400-N_3 and TSA-PEG5000-N_3 with different molecular weight of PEG linker (Supporting Information Scheme S1) and characterized them using ^{1}H NMR, ^{13}C NMR, MALDI-TOF-MS and FTIR (Supporting Information Fig. S11-S16). FITC-modified analogues TSA-PEG3400-N_3-FITC and TSA-PEG5000-N_3-FITC were used for quantitative anchoring analysis.

Notably, we found that the PEG linker of anchoring lipid exerted dual effects in the anchoring process. On the one hand, increasing PEG molecular weight enhanced the hydrophilicity of anchor lipids as well as the steric hindrance to hinder the insertion of the hydrophobic moiety into membrane. We demonstrated that the CMCs of anchoring lipids raised as the increase of PEG molecular weight measured via pyrene fluorescence assays (Fig. 3A and Supporting Information Table S2). Consistent with this, anchoring lipids with lower PEG molecular weights exhibited stronger membrane association at equal concentrations with higher fluorescence intensity (Fig. 3B, Supporting Information Fig. S18A), indicating that reduced hydrophilicity of anchor lipid promoted the interaction with membrane. On the other hand, higher-molecular-weight PEG linker inhibited the cellular endocytosis, in line with the previous reports [31,32]. A trypan blue quenching assay was used to differentiate membrane-anchored from internalized fractions of NEs. The results showed that anchor lipids with higher PEG molecular weights significantly reduced cellular uptake (Fig. 3C). Although TSA-PEG2000 displayed efficient membrane insertion, its weaker resistance to cellular uptake versus the higher-molecular-weight analogs (PEG3400 and PEG5000) led to a significant internalization by NEs, thereby reducing its membrane retention (Fig. 3D). Especially, TSA-PEG3400-N_3 demonstrated the strongest membrane anchoring, reaching 2.04 nmol/10^6 cells even after multiple washes (Fig. 3D, Supporting Information Fig. S18B).

We next investigated anchoring stability by incubating the anchored cells in culture medium for 8 h and monitoring membrane retention over time. The internalized fraction was quantitatively subtracted to accurately determine the amount of membrane-anchored molecules. The results showed that TSA-PEG3400 displayed superior membrane-

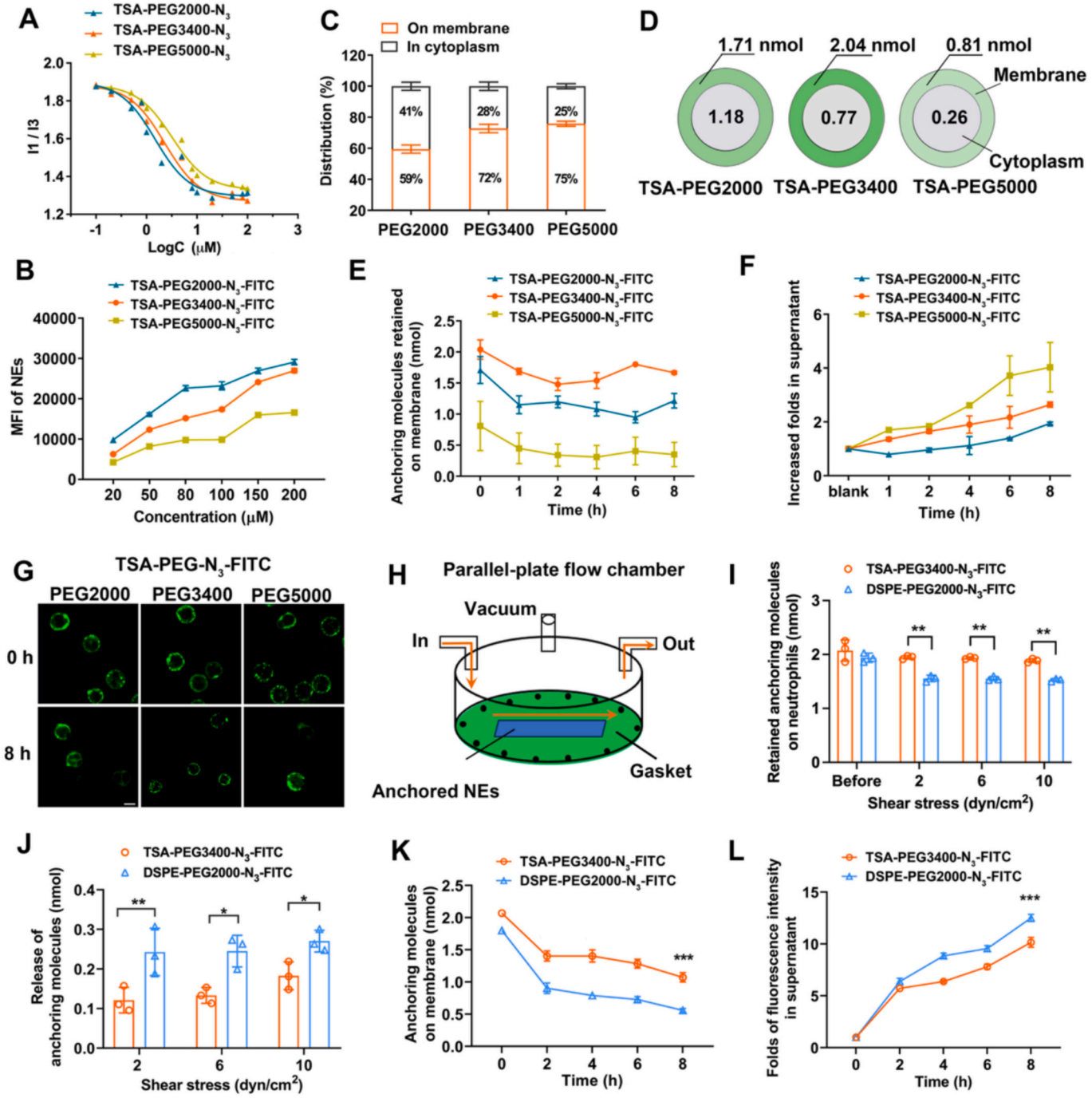

Fig. 3. Influence of hydrophilic group of trident membrane-anchoring lipid on the anchoring efficiency and stability of NEs. (A) The CMC of TSA-PEG-N_3 (MW = 2000, 3400, 5000 Da) with different molecular weight of PEG. (B) The fluorescence intensity on NEs after incubation with different concentrations of TSA-PEG-N_3-FITC. (C—D) The distribution ratio and amount of TSA-PEG-N_3 on NE membrane and in the cytoplasm. (E-F) The amount of anchoring molecules retained on membrane (E) and released to the culture supernatant with time (F), and the corresponding fluorescence distribution on cell membrane as observed by confocal microscope (G). Scale bar is 10 μm. (H-J) The effect of shearing force from different blood flow velocity on the stability of TSA-PEG3400-N_3-FITC on NEs (1×10^6) by parallel-plate flow chamber (H). The flowing direction is indicated by the orange arrows in (H). The two-tailed lipid DSPE-PEG2000-N_3-FITC was used as control. The retained amount of anchoring molecules on membrane per 10^6 NEs (I) and the released amount after shearing force (J). (K-L) The retained amount of anchoring molecules on membrane per 10^6 NEs (K) and the quantified release in external medium (L) after NEs stimulated by 10 nM bacterial peptide N-formyl-Met-Leu-Phe (fMLP). Data are mean ± SD ($n = 3$). The statistical analysis was performed by Two-way ANOVA in (I-L). $^*P < 0.05$, $^{**}P < 0.01$, $^{***}P < 0.001$.

binding stability compared to both TSA-PEG2000 and TSA-PEG5000, with reduced detachment and higher membrane retention (Fig. 3E-G). We attributed this to its optimal balance between membrane insertion capacity and resistance to cellular uptake. To precisely delineate the contribution of the trident lipid structure to anchoring stability, we also compared TSA-PEG3400 with DSPE-PEG3400 sharing the same PEG linker length. The markedly enhanced stability of TSA-PEG3400 versus DSPE-PEG3400 confirmed the decisive role of trident structure in promoting stable insertion (Supporting Information Fig. S19). Notably, within the DSPE-based series, DSPE-PEG2000 outperformed DSPE-PEG3400 in membrane retention, suggesting a more favorable trade-off between insertion capability and resistance to phagocytic

internalization (Supporting Information Fig. S19). Therefore, we adopted DSPE-PEG2000 as the benchmark for subsequent evaluations of TSA-PEG3400, ensuring a direct comparison with our earlier research framework [8]. Notably, TSA-PEG3400 demonstrated a 1.5-fold higher membrane retention after 8 h compared to DSPE-PEG2000 (Supporting Information Fig. S19), further confirming the superior stability.

Since the anchoring stability of TSA-PEG3400 would undergo various physiological challenges, the conditions including blood shear stress, trans-endothelial migration, and inflammatory stimulation were performed to further demonstrate the advantages of TSA-PEG3400 in anchoring stability. As NEs adhered to the endothelium, shear stress can promote the shedding of membrane-anchored lipids. Using a parallel-plate flow chamber to simulate this force (Fig. 3H), TSA-PEG3400-N_3-FITC exhibited significantly less shedding and greater retention than DSPE-PEG2000-N_3-FITC (Fig. 3I, J), demonstrating superior resistance to blood shear stress. Moreover, during NEs migrating across the endothelial cell layer, endothelial cells can internalize a portion of the N*E*-anchored lipids. Using a transwell chamber, TSA-PEG3400-N_3-FITC showed significant higher retention and lower internalization by endothelial cells, indicating its superior stability during transmigration (Supporting Information Fig. S20). In addition, under inflammatory stimulation, known to boost the release of membrane anchors, TSA-PEG3400-N_3-FITC displayed markedly less shedding than DSPE-PEG2000-N_3-FITC, likely attributable to its stronger membrane binding (Fig. 3K, L).

Collectively, we identified the optimal TSA-PEG3400-N_3 holding the superior anchoring stability on NE surface due to the improved hydrophobic interaction and the suitable PEG linker, which implied its strong potential in potentiating the stability of drug conjugation.

3.3. *Establishment of responsive NE-liposome conjugates via trident lipid-mediated anchoring-conjugation strategy*

Building upon the optimized TSA-PEG3400-N_3 anchoring lipid, we next investigated its capability for stable drug conjugation to NEs. Neutrophils exhibit strong natural tropism toward inflamed tumor vasculature and are rapidly recruited to sites of vascular inflammation, which renders them highly efficient for acute, site-specific drug delivery to tumor vessels, with clear advantages in targeting speed and specificity over other immune cells [33]. Accordingly, we applied neutrophils to achieve precise vascular-targeted delivery of anti-angiogenic agents.

Triple-negative breast cancer (TNBC) remains deficient in effective targeted anti-angiogenic therapies, while the PI3K/AKT/mTOR pathway is aberrantly activated in over 60% of TNBCs and critically drives pathological angiogenesis and tumor progression [34,35]. Among PI3K isoforms, PI3Kα (encoded by PIK3CA) is the most frequently mutated and directly mediates aberrant vascular formation, representing a rational anti-angiogenic target [36]. Notably, APLS, a selective PI3Kα inhibitor, is clinically approved for PIK3CA-Related Overgrowth Spectrum (PROS) disorders that involve pathological vascular malformations [37]. On this basis, we selected Alpelisib (APLS) as our model anti-angiogenic drug to suppress tumor neovascularization and induce tumor regression. To enable both convenient loading and tumor site-responsive release, APLS was encapsulated in liposomes that also incorporated an MMP9-cleavable lipid (DBCO-PLGLAG-SA_2, Supporting Information Fig. S21). This lipid breakage by upregulated MMP9 from activated vascular endothelial cells in the tumor microenvironment could trigger the subsequent release of the encapsulated drug. The resulting liposomal APLS (Lipo/APLS) exhibited a uniform spherical morphology with an average diameter of ~120 nm and a zeta potential of −10 mV. Moreover, Lipo/APLS demonstrated stable drug-loading under different external conditions (Supporting Information Fig. S22A-C). Subsequently, Lipo/APLS was conjugated onto NEs pre-anchored with TSA-PEG3400-N_3, yielding the NE-liposome conjugates (Lipo/APLS@NEs). The construction process was sequentially optimized by varying APLS concentration and incubation time. We found increased APLS concentration or longer incubation resulted in greater conjugation of rhodamine B-labeled Lipo/APLS and higher APLS loading per 10^6 NEs (Supporting Information Fig. S22D-H). Notably, the Lipo/APLS conjugation reach a plateau at an APLS concentration of 100 μg/mL and an incubation time of 30 min, in which Lipo/APLS demonstrated maximum conjugation effect while preserving NEs viability (Supporting Information Fig. S22F). Under this condition, we observed strong fluorescence colocalization between TSA-PEG3400-N_3-FITC and Rho B-liposomes, while unanchored NEs only displayed weak non-specific adsorption, further confirming successful anchoring-conjugation on cell surface (Fig. 4A, B). The drug-loading quantification suggested about 4 μg APLS carried on NEs (1×10^6) (Supporting Information Fig. S23A), and this anchoring-conjugation method could maintain a stable drug loading (>3.2 μg/10^6 NEs) on NEs for at least 8 h in culture medium (Fig. 4C).

To precisely delineate the contribution of TSA-PEG3400-N_3 anchoring to drug-conjugation stability, the two-tailed DSPE-PEG2000-N_3 anchoring herein was applied to conjugate liposomes as a contrast. Both anchoring-conjugation strategies showed no significant differences in drug-loading capacity (Supporting Information Fig. S23). Given that the system Lipo/APLS@NEs need to specifically deliver drugs to the tumor blood vessels, we thus primarily evaluated the drug-conjugation stability under the situation of blood flow shear and inflammation stimulation. As the shear force increased, TSA-PEG3400-N_3-mediated drug conjugation demonstrated higher retention compared to that mediated by DSPE-PEG2000-N_3 (Fig. 4D), indicating the more stable drug conjugation by TSA-PEG3400-N_3 enable withstand the impact of shear force. Furthermore, under strong inflammatory stimulation, the enhanced membrane binding of TSA-PEG3400-N_3 ensured a sustained drug release mode, with approximately 53% of drugs, equivalent to about 2.2 μg APLS retained on cells after 8 h (Fig. 4E). These data exhibited the superior drug-conjugation stability mediated by TSA-PEG3400-N_3 than DSPE-PEG2000-N_3, indicating enhanced hydrophobic interaction between anchors and cell membrane directly led to improved stability of its drug conjugate.

Having confirmed the enhanced drug-binding stability mediated by TSA-PEG3400-N_3 anchoring, we next evaluated its potential impact on NE biological functions. Despite almost unaffected cell vitality after Lipo/APLS conjugation compared to blank NEs during in vitro culture of 8 h (Fig. 4F), the cell membrane state such as membrane integrity and fluidity might potentially be compromised by membrane anchoring and drug conjugation [38], thereby interfering with membrane-dependent physiological activities. We found that at TSA-PEG3400 anchoring levels below 2.9 nmol per 10^6 NEs, neither membrane permeability (assessed by LDH release) nor membrane lipid fluidity showed significant changes within 8 h (Supporting Information Fig. S24). However, excessive anchoring (4.4 nmol per 10^6 NEs) increased membrane permeability, as evidenced by elevated LDH release at 8 h (Supporting Information Fig. S24A). Therefore, Lipo/APLS conjugation was operated based on 2.4 nmol TSA-PEG3400-N_3 anchoring on per 10^6 NEs, on which condition Lipo/APLS conjugation did not further perturb NE membrane permeability or fluidity (Fig. 4G, H). We next addressed whether conjugated liposomes sterically blocked membrane protein recognition or disrupted cell polarization, thus hindering cell migration. Reassuringly, the surface expression levels of key membrane proteins including CD11b, CXCR2, PSGL-1 and CD62L indicated unaltered after liposome conjugation (Fig. 4I, J). The cell polarization capacity essential for migration, which was assessed via fMLP-stimulated cytoskeletal protein (F-actin) redistribution, also demonstrated insignificant change (Fig. 4K). Since membrane proteins mediated the NEs response to inflammatory cytokines, and cell polarization ensured the amoeboid migration [39], the chemotaxis migration of NEs post-conjugation showed negligibly alteration according to the chemotactic index (Fig. 4L). Furthermore, given mature NEs rely predominantly on glycolysis due to minimal mitochondria [40], the metabolic function was also evaluated through glycolysis stress tests (using Seahorse Analyzer), which showed nearly identical extracellular acidification rate

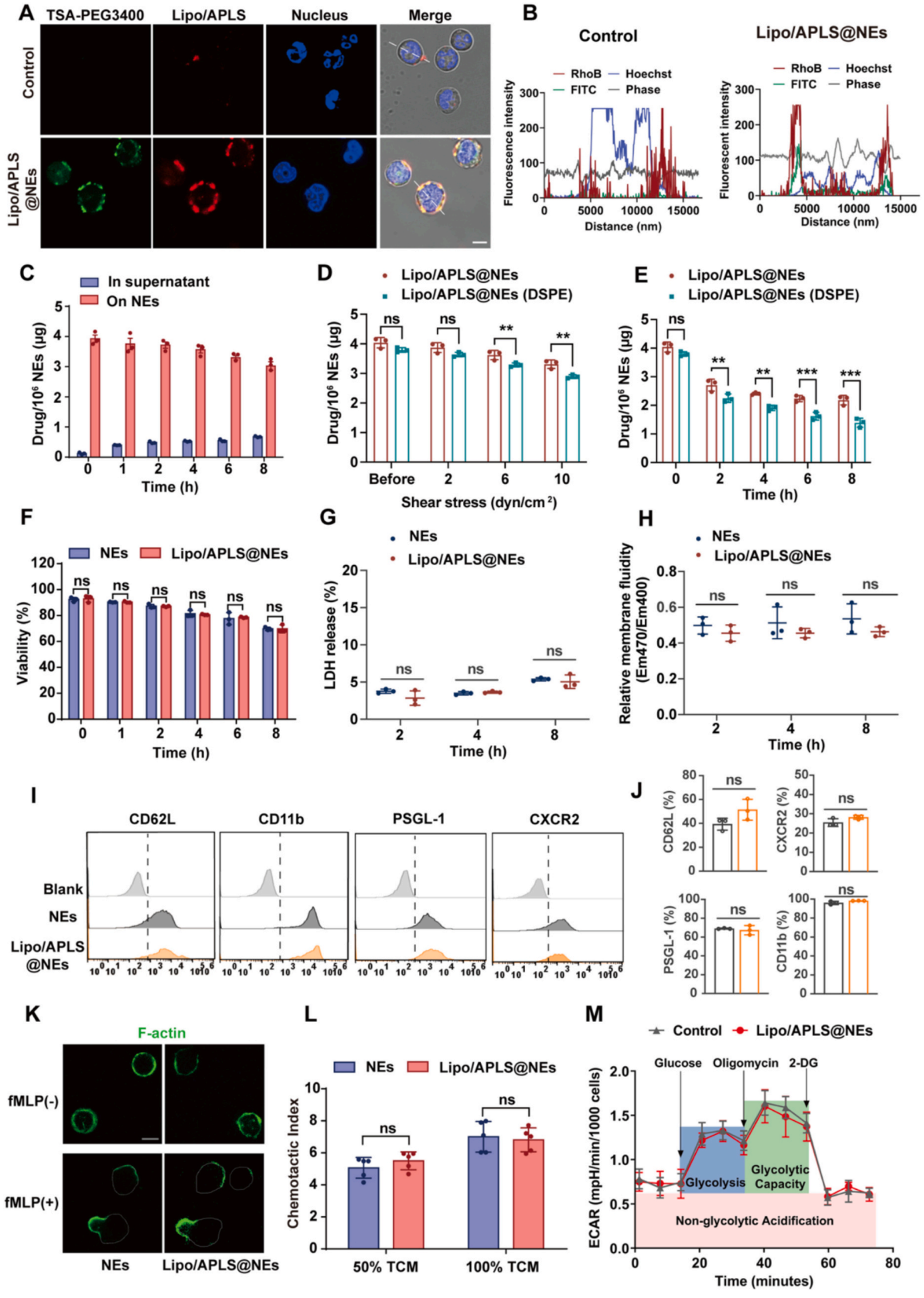

(caption on next page)

Fig. 4. Establishment of responsive NE-liposome conjugates via trident lipid-mediated anchoring-conjugation strategy. By default，Lipo/APLS@NEs represented the conjugates constructed by TSA-PEG3400-N_3-anchoring. (A-B) The fluorescence co-localization between Rho B-labeled liposomes and TSA-PEG3400-N_3-FITC anchoring on NEs, indicating successful conjugation of liposomes on NE membrane. The fluorescence intensity in (B) was measured along the white line in (A). Scale bar, 5 μm. (C) The drug-loading stability of Lipo/APLS@NEs in culture medium containing 10% FBS ($n = 3$). Lipo/APLS@NEs (DSPE) were the control conjugates constructed by DSPE-PEG2000-N_3-anchoring for comparison of drug-conjugation stability. (D-E) The drug-loading stability of Lipo/APLS@NEs under the shearing force of blood flow (D) and inflammation stimulation (E). (F) The influence of Lipo/APLS conjugation on cell viability. (G-H) The effect of Lipo/APLS conjugation on cell membrane functions including membrane permeability (G) and membrane lipid fluidity (H). (I-M) The cell migration functions including the expression of key membrane proteins (I-J), cell polarization (K) and chemotactic migration (L) under the recruitment of fMLP. Scale bar, 5 μm. (M) The glycolysis stress test on Seahorse quantified by ECAR. Data in (M) are mean ± SD ($n = 12$). Data shown in (L) are mean ± SD ($n = 5$). Data shown in (C-J) are mean ± SD (n = 3). The statistical analysis was performed by Two-way ANOVA in (D—H, L) and Student's *t*-test in (J). $^{**}P < 0.01$ and $^{***}P < 0.001$. ns meant not significant.

(ECAR) profiles between conjugated and blank NEs after sequential substrate injections, confirming unaltered glycolytic function (Fig. 4M). Taken together, TSA-PEG3400-N_3-mediated liposomal APLS attachment exerted no significant impact on NE physiological functions, suggesting the therapeutic application potentials.

In summary, we successfully established a NEs-drug conjugate Lipo/APLS@NEs using TSA-PEG3400-N_3-mediated anchor-conjugation strategy, which achieved significantly enhanced drug-conjugation stability for cell-based drug delivery compared to previous anchors.

3.4. *In vitro anti-angiogenic efficacy of Lipo/APLS@NEs via MMP9-responsive drug release*

The stimuli-responsive capability of the NEs-drug conjugate Lipo/APLS@NEs was systematically evaluated. Firstly we evaluated the change of Lipo/APLS after MMP9 treatment, which indicated a slight size reduction and no distinct morphological change, accompanied by a limited increase in drug leakage (Supporting Information Fig. S25). This suggested that MMP9-mediated cleavage of the responsive peptide induced size decrease without substantially compromising liposomal integrity, thereby resulting in minimal drug leakage. Next the responsive release profile of Lipo/APLS@NEs was quantified by measuring APLS in the culture supernatant. Approximately 80% cumulative release occurred within 8 h under MMP9 conditions, whereas less than 20% was released in its absence (Fig. 5A), clearly demonstrating the MMP9-responsive drug release capability of Lipo/APLS@NEs.

Before exploring the MMP9-responsive release behavior of Lipo/APLS@NEs in vivo, we first explored the tumor-targeting ability of Lipo/APLS@DIR-labeled NEs in 4 T1 breast tumor-bearing mice. By an in vivo imaging system (IVIS), we observed that Lipo/APLS@NEs effectively accumulated at tumor site probably due to the NE tendency to activated tumor vessels, which showed no significant difference in tumor-targeting efficiency with blank NEs (Fig. 5B, Supporting Information Fig. S26A). Moreover, liposome conjugation had no effect on the biodistribution of NEs (Supporting Information Fig. S26B, C), suggesting the unchanged physiological function of NEs. Furthermore, the APLS concentration in typical organs and tumors was detected by HPLC to further confirm the tumor targeting ability. The results showed that Lipo/APLS@NEs significantly reduced the non-specific distribution of APLS in normal organs such as the liver, spleen, and lung (Supporting Information Fig. S26D), while increasing APLS accumulation in tumors to 1.6-folds of free APLS liposomes (Fig. 5C). The enhanced tumor accumulation could be attributed to the inherent tendency of NEs to migrate toward tumor vasculature.

For better understanding the specific release of APLS liposomes from Lipo/APLS@NEs at tumor vascular, we observed the tumor tissue cryosections at different post-injection time points. Meanwhile, the non-responsive Lipo-APLS@NEs was prepared using liposomes incorporated with DBCO-SA_2 without MMP9-cleavable part as a control. Lipo/APLS@NEs exhibited time-dependent adhesion on tumor vasculature endothelium, and the colocalization of APLS liposomes and NEs gradually separated around tumor vasculature. Conversely, non-responsive Lipo-APLS@NEs revealed co-localization of APLS liposomes with adherent NEs in vessel wall (Fig. 5D, E). These data confirmed the specific release of Lipo/APLS from NE-liposome conjugates at tumor vascular, which would be beneficial to the improved efficacy of loaded drugs.

Based on the site-specific drug release, the anti-angiogenesis potency of Lipo-APLS@NEs in vitro was evaluated. We firstly established an activated vascular endothelial cell model by TNFα stimulation, which showed an evidently increased expression of adhesion molecules VCAM-1 and elevated release of MMP9 (Supporting Information Fig. S27). Leveraging this model, we found the secreted MMP9 triggered rapid APLS release, leading to significant suppression of endothelial cell proliferation and migration, an efficacy matching that of free APLS (Fig. 5F-I). While in the absence of MMP9, Lipo/APLS@NEs generated a slight inhibition on the migration of vascular endothelial cells comparable to controls, as the drug failed to be released promptly (Fig. 5G-I). Notably, Lipo/APLS@NEs without MMP9 stimulation still generated markedly inhibition on the proliferation, which was mainly due to the drug leakage from the apoptotic NEs during the 48-h observation period. However, the inhibitory effect on proliferation was still weaker than that triggered by MMP9 owing to the delayed drug release (Fig. 5F). Based on these, Lipo/APLS@NEs could lead to effective inhibition for vascular network formation after MMP9 treatment (Fig. 5J-M). These results comprehensively validated the MMP9-responsive drug release capability of Lipo/APLS@NEs, which led to potent anti-angiogenic efficacy in vitro.

3.5. *Improved therapeutic efficacy of MMP9-responsive NE-liposome conjugates*

To evaluate the in vivo treatment efficacy of NE-liposome conjugates, an orthotopic breast cancer mouse model was performed. Following the predefined treatment regimen, the MMP9-responsive Lipo/APLS@NEs and other formulations was respectively administered intravenously or by daily gavage (Fig. 6A). The results showed that the responsive Lipo/APLS@NE significantly suppressed the tumor growth compared to other groups, as monitored via bioluminescence imaging (IVIS Spectrum) and tumor volume (Fig. 6B-D) along with a marked reduction in tumor weight (Fig. 6E). The enhanced performance could be attributed to the MMP9-responsive release at tumor vascular, which promoted local drug bioavailability. This was further confirmed by the superior inhibition on tumor angiogenesis achieved by MMP9-responsive Lipo/APLS@NEs than the non-cleavable Lipo-APLS@NE (Fig. 6F, G). By disrupting the supply of oxygen and nutrients, this enhanced anti-angiogenic effect effectively induced tumor starvation. Based on that, the mice treated with Lipo/APLS@NEs exhibited a 1.2-fold prolongation in survival relative to those receiving the non-responsive counterpart (Fig. 6H), which was probably benefited from the suppression of vascularization contributing to the impaired tumor growth. These collective findings indicated that the enhanced tumor targeting of NEs and rapidly release of APLS liposomes at tumor vascular endothelium contributed to a pronounced antitumor effect.

In addition to the enhanced antitumor performance, Lipo/APLS@NEs also exhibited a favorable biosafety profile. Throughout the study, no significant signs of systemic toxicity of Lipo/APLS@NEs were observed compared with other group, as indicated by stable body weight, normal liver and kidney function markers (AST, ALT, CRE, BUN), balanced organ-to-body weight ratios, and the absence of

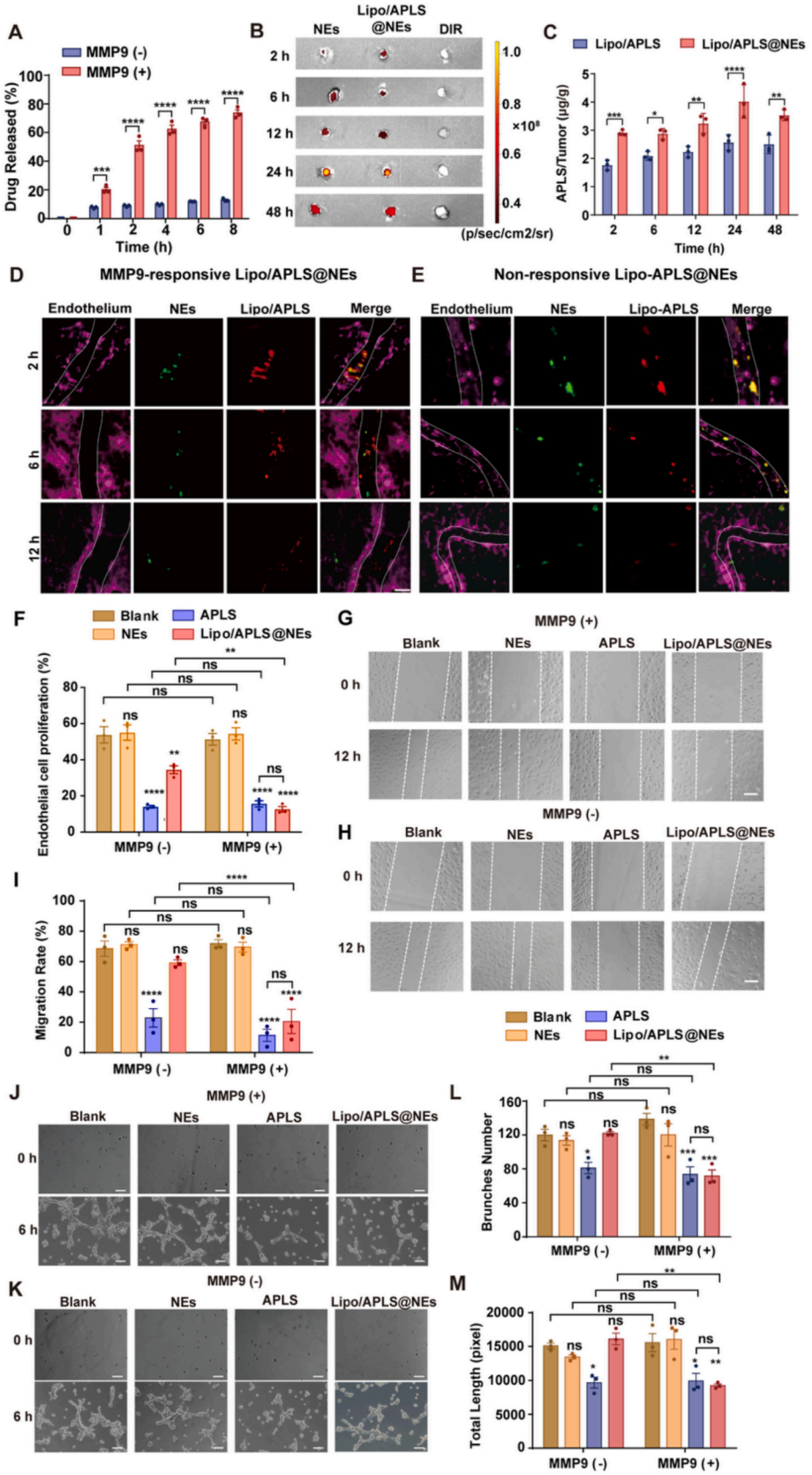

(caption on next page)

Fig. 5. In vitro anti-angiogenic efficacy of Lipo/APLS@NEs via MMP9-responsive drug release. (A) The boosted APLS release of Lipo/APLS@NEs stimulated by 20 nM MMP9 ($n = 3$). (B) The in vivo biodistribution of Lipo/APLS@NEs in tumors at different time after i.v. administration (n = 3 mice per group). The blank NEs and free DIR dye were set as control. (C) The APLS accumulation in tumors were quantified by HPLC (n = 3 mice per group). (D-E) The responsive drug release of Lipo/APLS@NEs inside tumor vessels over time, from initial NEs (green) adhesion followed by MMP9-responsive liposome (red) release within tumor vessels (magenta) after i.v. administration. Here Lipo-APLS@NEs indicated NE-liposome conjugates without MMP9-sensitive peptide. Scale bar, 50 μm. (F) In vitro anti-proliferation efficacy of Lipo/APLS@NEs on SVEC4–10 cells. The blank endothelial cells SVEC4–10 treated by blank NEs or free APLS were as controls. (G-I) The in vitro inhibition effect on invasion rate of SVEC4–10 cells. Scale bar, 20 μm. The scratch recovery rate for evaluating the migration of SVEC4–10 cells was calculated with the initial and final scratch area as measured by Image J. (J-K) The in vitro inhibition on neovascularization of SVEC4–10 cells. Scale bar, 20 μm. The branch numbers (L) and total length (M) of the neovascularization were analyzed from random three fields by image J. All data were mean ± SD (n = 3). The statistical analysis was performed by Two-way ANOVA. $^{*}P < 0.05$, $^{**}P < 0.01$, $^{***}P < 0.001$, $^{****}P < 0.0001$ and ns, not significant. (For interpretation of the references to colour in this figure legend, the reader is referred to the web version of this article.)

pathological injury in major organs (Supporting Information Fig. S28). These results implied the potential of Lipo/APLS@NEs for clinical translation.

Collectively, Lipo/APLS@NEs, featuring strengthened drug-conjugation stability and enzyme-triggered release, demonstrated superior antitumor efficacy via potent suppression of tumor growth and angiogenesis, alongside a favorable safety profile, underscoring significant clinical translational potential.

3.6. The in vivo advantages of trident anchor-conjugation strategy compared to double-tailed anchor-conjugation strategy

For deep understanding the contribution of trident anchor-conjugation strategy to therapeutic outcomes, we systematically evaluated the responsive NE-liposome conjugates anchored by TSA-PEG3400-N_3 or DSPE-PEG2000-N_3 in orthotopic breast cancer models (Fig. 7A). TSA-PEG-N_3-mediated Lipo/APLS@NEs (TSA) exhibited significantly higher APLS accumulation in tumors, approximately 1.3-fold greater than Lipo/APLS@NEs (DSPE) at the 24-h time point (Fig. 7B). This indicated the strengthened anchoring could deliver more drugs to tumor sites based on the active targeting of NEs and the MMP9-responsive drug release mechanism, thereby supporting superior therapeutic effects. This was further verified by in vivo tumor suppression effect. According to the predefined treatment regimen (Fig. 7C), Lipo/APLS@NEs by TSA-PEG anchoring resulted in significantly potentiated suppression of tumor growth, as evidenced by weakened bioluminescence imaging (IVIS Spectrum) and delayed tumor growth kinetics (Fig. 7D-F). Moreover, we found the increased APLS accumulation in tumor vessels via Lipo/APLS@NEs (TSA) could translate to enhanced inhibition on tumor angiogenesis (Fig. 7G, H), which in turn reduced the supply of oxygen and nutrients, thereby leading to suppressive tumor cell proliferation (Ki67 immunohistochemistry) and lessened tumor weight compared to Lipo/APLS@NEs (DSPE) (Fig. 7I, J). Accordingly, Lipo/APLS@NEs (TSA) achieved a prolonged survival with a 1.2-fold extension compared to Lipo/APLS@NEs (DSPE) (Fig. 7K). These findings collectively underscored the critical role of stable drug conjugation mediated by TSA-PEG-N_3 in maximizing therapeutic efficacy.

4. Discussion

Current strategies for non-covalent attachment of therapeutic agents to cell surfaces most commonly rely on receptor-ligand interactions. This method, while specific, lacks generalizability as it necessitates bespoke design for each cell type based on its unique receptor expression profile [41]. Another strategy, electrostatic adsorption often suffers from instability as the attached payloads can be readily displaced by competing ions or serum proteins. In contrast, the anchoring-conjugation strategy circumvents these constraints through a modular architecture comprising a hydrophobic membrane anchor, a hydrophilic linker, and a terminal reactive group. The modular design allows tailored adaptation to different cells and payloads, providing a universal framework for diverse cell-drug conjugates.

Capitalizing on this versatility, our group has used the classical two-tailed phospholipid anchor (DSPE-PEG) to engineer drug-carrying T cells and NEs. As for the phagocytic NEs, earlier work involved pre-loading NEs with nanodrugs to partially saturate phagocytosis before surface drug conjugation, thus increasing the conjugation efficiency [8]. To further improve clinical feasibility, this study investigated direct drug anchoring onto the NE surface without prior saturation of endocytosis. This presented two main challenges: active endocytic activity that internalizes surface cargo, and high membrane fluidity—essential for phagocyte function—that promotes premature payload release, a general obstacle in cell-based drug delivery. To address these issues, we developed a biomimetic trident membrane-anchoring lipid, TSA-PEG3400-N_3, inspired by the stable membrane association of sperm-related GPI-anchored proteins. The triple-tail design strengthened hydrophobic interactions with the NEs membrane, improving drug retention without compromising cell viability or function. For minimizing cellular uptake while maximizing surface attachment efficiency, we systematically optimized the PEG linker length and conjugation condition. The resulting TSA-PEG3400-N_3 anchor showed superior stability under physiological conditions, outperforming the conventional two-tailed DSPE-PEG anchor.

Furthermore, the modularity of this strategy allows integration of stimulus-responsive linkers for controlled drug release, catering to specific therapeutic needs. In this work, we incorporated a matrix metalloproteinase-9 (MMP9)-cleavable linker between the anchor and the liposomal drug (Alpelisib) payload. Since MMP9 is overexpressed in tumor vasculature [42], this design ensured drug retention during systemic circulation but triggered rapid, site-specific release upon NE adhesion to activated tumor endothelium. The delivered PI3Kα inhibitor, Alpelisib, then potently inhibited angiogenesis, cutting off the tumor nutrient supply. This synergy between NE-mediated targeted delivery and microenvironment-triggered precise release resulted in enhanced intra-tumoral drug accumulation, potent anti-angiogenic effects, and significant tumor suppression. Critically, the improved drug-conjugation stability mediated by TSA-PEG3400-N_3, compared to previously used DSPE-PEG, directly translated to greater drug delivery and stronger antitumor efficacy, validating that enhancing hydrophobic interaction strength was a viable strategy to boost therapeutic outcomes. Further, improved drug-conjugation stability by TSA-PEG3400-N_3 can allow similar efficacy with lower doses or less frequent administration, improving patient compliance and safety by minimizing off-target exposure.

Despite the marked improvement, this study only attenuated but did not abolish the internalization of surface-conjugated drugs by NEs, a design that intentionally preserved the NEs' essential native migratory and phagocytic functions. Although the adoptively transferred NEs from healthy donor mice have been shown to lack inherent immunosuppressive properties, the phenotypic fate and functional dynamics of these NEs within the complex tumor immune microenvironment remain to be elucidated. Future studies will focus on elucidating the in vivo polarization status and fate of these NEs post-transfer to comprehensively validate their immune safety profile. Furthermore, our trident anchoring lipid-mediated strategy could be extended with multi-stimuli-responsive linkers and adapted to other phagocytic or non-phagocytic cells, broadening its applicability in cell-based combination therapies.

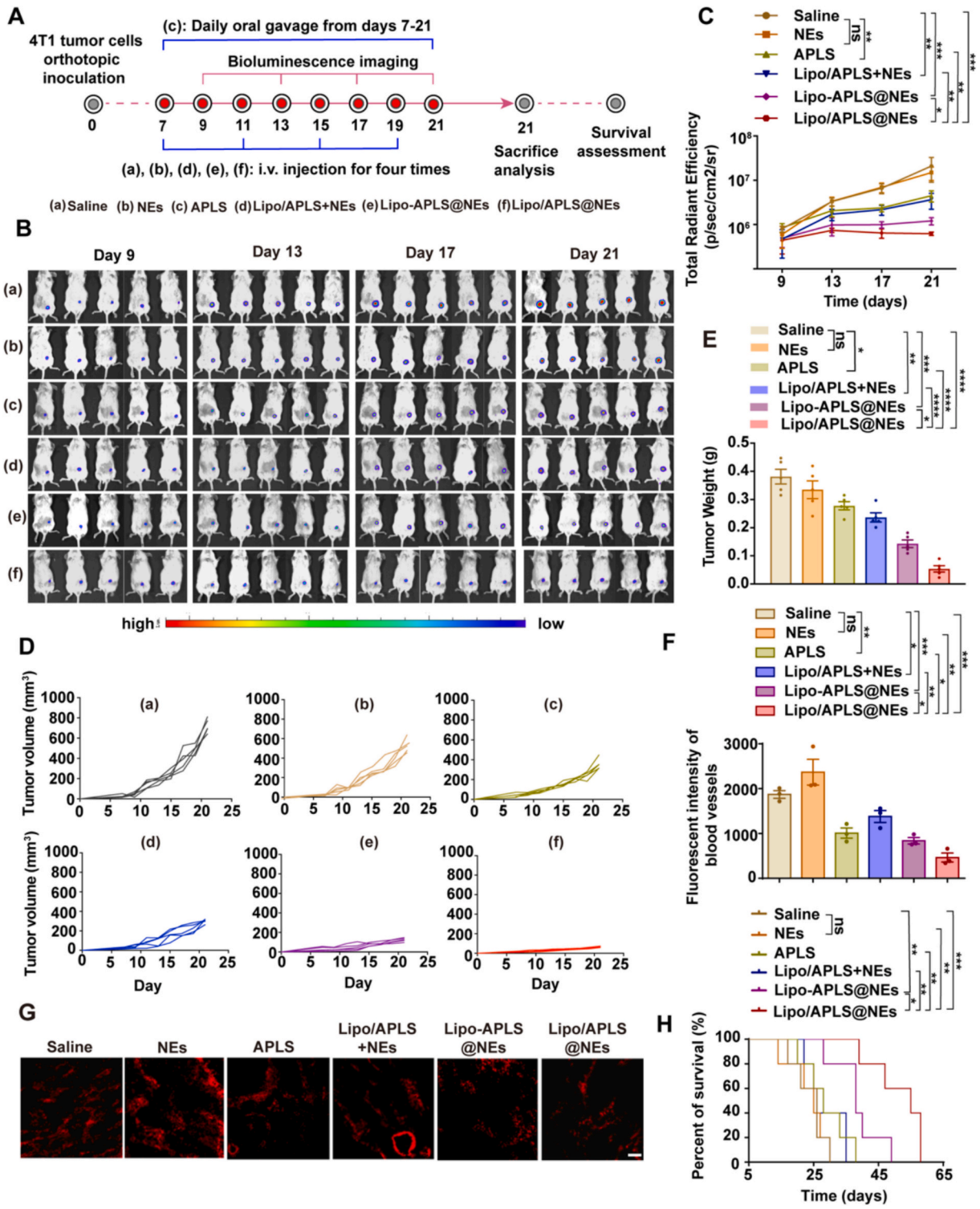

Fig. 6. Improved therapeutic efficacy of MMP9-responsive NE-liposome conjugates in vivo. (A) Schematic illustration of the experimental timeline for anti-tumor efficacy studies in orthotopic tumor-bearing mice. Saline, blank NEs (NEs, 2×10^7 cells), the combination of liposome Lipo/APLS (APLS 4 mg/kg) and NEs (2×10^7 cells), the non-responsive Lipo-APLS@NEs (2×10^7 cells) and the MMP9-responsive Lipo/APLS@NEs (2×10^7 cells) were administered intravenously on days 7, 11, 15, and 19 post-inoculation. Free APLS (20 mg/kg) was administered by daily gavage from Day 7 to Day 21 after tumor inoculation. (B—C) The 4 T1 breast tumor growth monitored through bioluminescence in IVIS Spectrum and (D) the tumor growth kinetics after different preparation treatment ($n = 5$ mice per group). (E) The tumor weight recorded after treatment completed (n = 5 mice per group). (F-G) The in vivo anti-angiogenesis effect after different treatment as showed by immunohistochemical frozen tumor sections (G). Scale bar, 100 μm. The quantitative fluorescence intensity of tumor vessels from random three frozen tissue sections of 4 T1 tumor-bearing mice after different treatment (F). (H) Tumor-bearing mice survival after different treatment (n = 5 mice per group). All Data were mean ± SD. The statistical analysis was performed by Two-way ANOVA in (C), Owo-way ANOVA in (E, F) and Log-rank (Mantel-Cox) test in (H). $^*P < 0.05$, $^{**}P < 0.01$, $^{***}P < 0.001$ and $^{****}P < 0.0001$. ns, not significant.

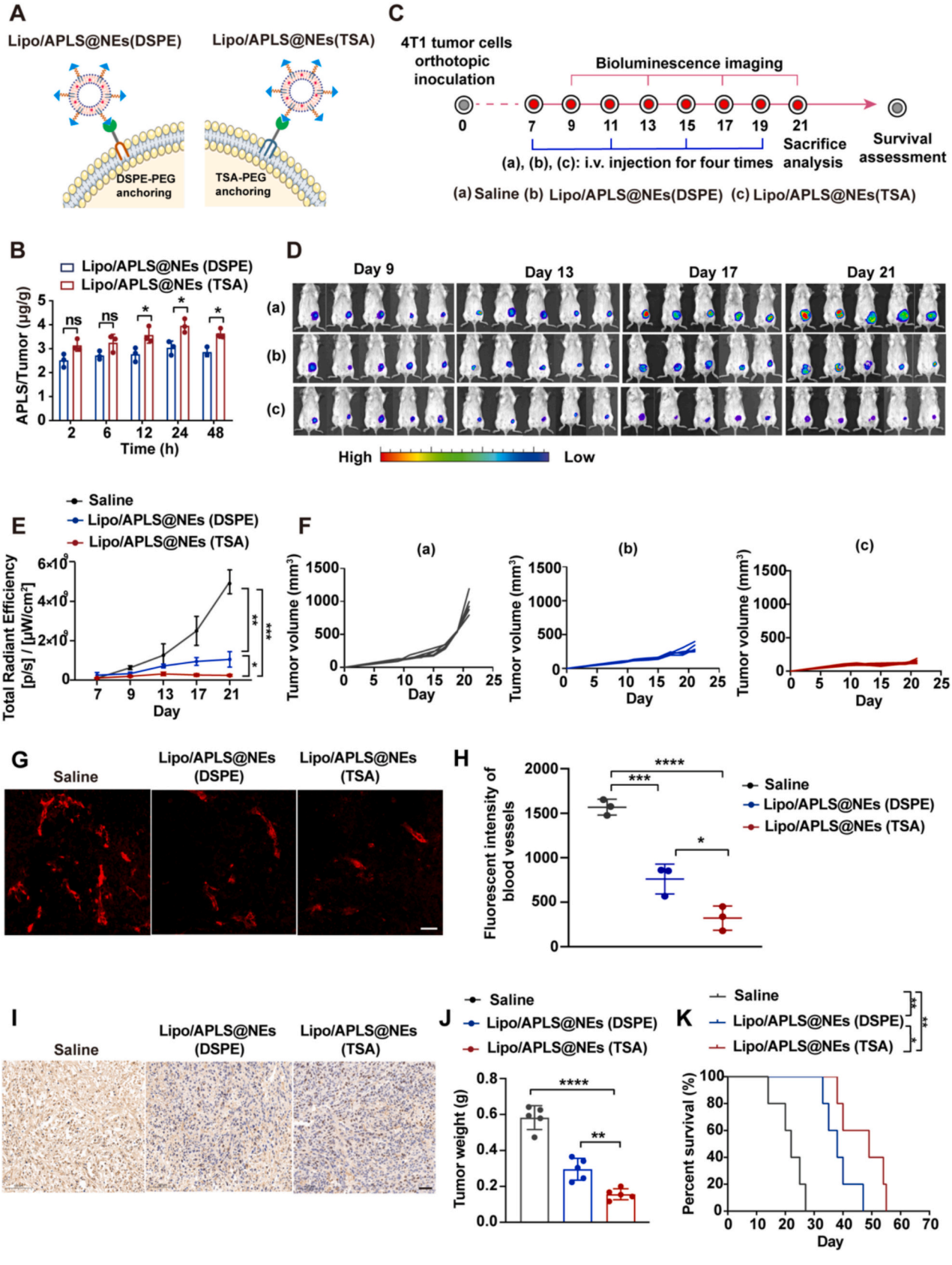

(caption on next page)

Fig. 7. The in vivo advantages of trident anchor-conjugation strategy compared to double-tailed anchor-conjugation strategy. (A) Construction of MMP9-responsive Lipo/APLS@NEs mediated by TSA-PEG3400-N_3 anchoring or DSPE-PEG2000-N_3 anchoring. (B) The obtained Lipo/APLS@NEs(TSA) and Lipo/APLS@NEs(DSPE) were respectively intravenously administered into orthotopic tumor-bearing mice (2×10^7 cells, equivalent to 80 μg of APLS each mouse). The APLS accumulation within tumors quantified via HPLC ($n = 3$ mice per group). (C) Schematic illustration of the anti-tumor efficacy studies from different anchoring-conjugation strategy in orthotopic tumor-bearing mice. The MMP9-responsive Lipo/APLS@NEs(TSA) and Lipo/APLS@NEs(DSPE) (2×10^7 cells) were administered intravenously on days 7, 11, 15, and 19 post-inoculation. (D-E) The tumor growth monitored through bioluminescence in IVIS Spectrum and the corresponding total radiant efficiency with time ($n = 5$ mice per group). (F) The tumor growth kinetic after different treatment (n = 5 mice per group). (G-H) The in vivo anti-angiogenesis effect after different treatment as showed by immunohistochemical frozen tumor sections (G). Scale bar, 50 μm. The quantitative fluorescence intensity of tumor vessels was analyzed from three random frozen tissue sections of each group by Image J (H). (I) The tumor proliferation assessed by Ki67 immunohistochemical staining. Scale bar, 100 μm. (J) The tumor weight measured after different treatment (n = 5 mice per group). (K) The mice survival after different treatment (n = 5 mice per group). Data were mean ± SD. The statistical analysis was performed by Two-way repeated measures ANOVA in (B, E), One-way ANOVA in (H, J) and Log-rank (Mantel-Cox) test in (K). $^*P < 0.05$, $^{**}P < 0.01$, $^{***}P < 0.001$ and $^{****}P < 0.0001$. ns, not significant.

5. Conclusion

In summary, we have established a robust and versatile cell-drug conjugation strategy based on a bioinspired trident anchoring lipid. This approach overcomes a key limitation in phagocyte-mediated drug delivery by strengthening membrane anchoring through enhanced hydrophobic interactions. Coupled with a tumor-microenvironment-responsive release mechanism, this system enables precise, effective and safe drug delivery to disease sites, holding significant clinical potential. This work establishes a generalizable strategy for stable and specific drug conjugation to diverse cell types, offering significant potential for advancing cell-based combination therapeutics.

CRediT authorship contribution statement

Luping Zhang: Visualization, Validation, Software, Methodology, Investigation, Formal analysis, Data curation, Conceptualization. **Yu Jin:** Visualization, Methodology, Investigation, Formal analysis. **Meixi Hao:** Methodology, Formal analysis, Data curation. **Yijun Chen:** Visualization, Software, Methodology, Investigation. **Yupeng Dai:** Visualization, Methodology, Investigation. **Mengtong Wu:** Methodology, Investigation, Formal analysis, Data curation. **Zihao Zhang:** Methodology, Investigation. **Tong Wu:** Investigation. **Luyao Fang:** Investigation. **Yujiao Wang:** Investigation. **Xiao Xu:** Software, Investigation, Formal analysis. **Caoyun Ju:** Writing – review & editing, Supervision, Formal analysis, Data curation. **Can Zhang:** Writing – review & editing, Supervision, Project administration, Funding acquisition.

Declaration of competing interest

The authors declare no competing interests.

Acknowledgements

This work was supported by the National Natural Science Foundation of China (82130102, 92159304, 81930099), the Natural Science Foundation of Jiangsu Province (BK20212011), the “Open Competition to Select the Best Candidates” Key Technology Program for Nucleic Acid Drugs of NCTIB (NCTIB2022HS01014), “Double First-Class” University project (CPU2022QZ05), National Major Scientific and Technological Special Project for “Significant New Drugs Development” (2019ZX09301163), and the Open Project of State Key Laboratory of Natural Medicines (China Pharmaceutical University, SKLNMZZ202310).

Appendix A. Supplementary data

Supplementary data to this article can be found online at https://doi.org/10.1016/j.jconrel.2026.114903.

Data availability

The data that support the findings of this study are available from the corresponding authors upon reasonable request.

References

[1] C.J. Bashor, I.B. Hilton, H. Bandukwala, D.M. Smith, O. Veiseh, Engineering the next generation of cell-based therapeutics, Nat. Rev. Drug Discov. 21 (2022) 655–675, https://doi.org/10.1038/s41573-022-00476-6.
[2] C. D'Avanzo, F. Blaeschke, M. Lysandrou, F. Ingelfinger, R. Zeiser, Advances in cell therapy: progress and challenges in hematological and solid tumors, Trends Pharmacol. Sci. 45 (2024) 1119–1134, https://doi.org/10.1016/j.tips.2024.10.016.
[3] S. Temple, Advancing cell therapy for neurodegenerative diseases, Cell Stem Cell 30 (2023) 512–529, https://doi.org/10.1016/j.stem.2023.03.017.
[4] T.L. Hunter, Y. Bao, Y. Zhang, D. Matsuda, R. Riener, A. Wang, J.J. Li, F. Soldevila, D.S.H. Chu, D.P. Nguyen, Q.-C. Yong, B. Ross, M. Nguyen, J. Vestal, S. Roberts, D. Galvan, J.B. Vega, D. Jhung, M. Butcher, J. Nguyen, S. Zhang, C. Fernandez, J. Chen, C. Herrera, Y. Kuo, E.M. Pica, G. Mondal, A.L. Mammen, J. Scholler, S. P. Tanis, S.A. Sievers, A.M. Frantz, G.B. Adams, L. Shawver, R. Farzaneh-Far, M. Rosenzweig, P.P. Karmali, A.I. Bot, C.H. June, H. Aghajanian, In vivo CAR T cell generation to treat cancer and autoimmune disease, Science 388 (2025) 1311–1317, https://doi.org/10.1126/science.ads8473.
[5] J. Xue, Z. Zhao, L. Zhang, L. Xue, S. Shen, Y. Wen, Z. Wei, L. Wang, L. Kong, H. Sun, Q. Ping, R. Mo, C. Zhang, Neutrophil-mediated anticancer drug delivery for suppression of postoperative malignant glioma recurrence, Nat. Nanotechnol. 12 (2017) 692–700, https://doi.org/10.1038/nnano.2017.54.
[6] Y. Liu, K. Adu-Berchie, J.M. Brockman, M. Pezone, D.K.Y. Zhang, J. Zhou, J. W. Pyrdol, H. Wang, K.W. Wucherpfennig, D.J. Mooney, Cytokine conjugation to enhance T cell therapy, Proc. Natl. Acad. Sci. USA 120 (2023) e2213222120, https://doi.org/10.1073/pnas.2213222120.
[7] C.W. Shields, M.A. Evans, L.L.-W. Wang, N. Baugh, S. Iyer, D. Wu, Z. Zhao, A. Pusuluri, A. Ukidve, D.C. Pan, S. Mitragotri, Cellular backpacks for macrophage immunotherapy, Sci. Adv. 6 (2020) eaaz6579, https://doi.org/10.1126/sciadv.aaz6579.
[8] L. Zhang, Q. Wang, Y. Dai, J. Chen, T. Wu, C. Ju, L. Xue, C. Zhang, New-generation cytopharmaceuticals with powerfully boosted extravasation for enhanced cancer therapy, J. Control. Release 359 (2023) 116–131, https://doi.org/10.1016/j.jconrel.2023.05.037.
[9] M. Gruijs, C.A.N. Sewnath, M. van Egmond, Therapeutic exploitation of neutrophils to fight cancer, Semin. Immunol. 57 (2021) 101581, https://doi.org/10.1016/j.smim.2021.101581.
[10] N.R. Anderson, N.G. Minutolo, S. Gill, M. Klichinsky, Macrophage-based approaches for cancer immunotherapy, Cancer Res. 81 (2021) 1201–1208, https://doi.org/10.1158/0008-5472.can-20-2990.
[11] L. Yang, Y. Yang, Y. Chen, Y. Xu, J. Peng, Cell-based drug delivery systems and their in vivo fate, Adv. Drug Deliv. Rev. 187 (2022) 114394, https://doi.org/10.1016/j.addr.2022.114394.
[12] M. Hao, L. Zhu, S. Hou, S. Chen, X. Li, K. Li, N. Zhu, S. Chen, L. Xue, C. Ju, C. Zhang, Sensitizing tumors to immune checkpoint blockage via STING agonists delivered by tumor-penetrating neutrophil cytopharmaceuticals, ACS Nano 17 (2023) 1663–1680, https://doi.org/10.1021/acsnano.2c11764.
[13] M. Hao, Y. Zhou, S. Chen, Y. Jin, X. Li, L. Xue, M. Shen, W. Li, C. Zhang, Spatiotemporally controlled T-cell combination therapy for solid tumor, Adv. Sci. 11 (2024) e2401100, https://doi.org/10.1002/advs.202401100.
[14] C. Wang, W. Sun, Y. Ye, Q. Hu, H.N. Bomba, Z. Gu, In situ activation of platelets with checkpoint inhibitors for post-surgical cancer immunotherapy, Nat. Biomed. Eng. 1 (2017) 0011, https://doi.org/10.1038/s41551-016-0011.
[15] Y. Wang, J. Shi, M. Xin, A.R. Kahkoska, J. Wang, Z. Gu, Cell-drug conjugates, Nat. Biomed. Eng. 8 (2024) 1347–1365, https://doi.org/10.1038/s41551-024-01230-6.
[16] W. Li, Z. Su, M. Hao, C. Ju, C. Zhang, Cytopharmaceuticals: an emerging paradigm for drug delivery, J. Control. Release 328 (2020) 313–324, https://doi.org/10.1016/j.jconrel.2020.08.063.
[17] A. Lamoot, A. Uvyn, S. Kasmi, B.G. De Geest, Covalent cell surface conjugation of nanoparticles by a combination of metabolic labeling and click chemistry, Angew. Chem. Int. Ed. 60 (2021) 6320–6325, https://doi.org/10.1002/anie.202015625.
[18] C. Johnbosco, M. Becker, N. Willemen, M. Meteling, K. Govindaraj, T. Kamperman, J. Leijten, Covalent on-cell conjugation of biomaterials through oxidative phenolic coupling regulates stem cell fate via intracellular biophysical programming, Adv. Funct. Mater. 35 (2025) 2418963, https://doi.org/10.1002/adfm.202418963.

[19] Y. Chen, X. Chen, W. Bao, G. Liu, W. Wei, Y. Ping, An oncolytic virus–T cell chimera for cancer immunotherapy, Nat. Biotechnol. 42 (2024) 1876–1887, https://doi.org/10.1038/s41587-023-02118-7.
[20] J.T. Wilson, V.R. Krishnamurthy, W. Cui, Z. Qu, E.L. Chaikof, Noncovalent cell surface engineering with cationic graft copolymers, J. Am. Chem. Soc. 131 (2009) 18228–18229, https://doi.org/10.1021/ja908887v.
[21] M. Hao, S. Hou, W. Li, K. Li, L. Xue, Q. Hu, L. Zhu, Y. Chen, H. Sun, C. Ju, C. Zhang, Combination of metabolic intervention and T cell therapy enhances solid tumor immunotherapy, Sci. Transl. Med. 12 (2020) eaaz6667, https://doi.org/10.1126/scitranslmed.aaz6667.
[22] J.V. Vermaas, E. Tajkhorshid, A microscopic view of phospholipid insertion into biological membranes, J. Phys. Chem. B 118 (2014) 1754–1764, https://doi.org/10.1021/jp409854w.
[23] M.F. Renne, R. Ernst, Membrane homeostasis beyond fluidity: control of membrane compressibility, Trends Biochem. Sci. 48 (2023) 963–977, https://doi.org/10.1016/j.tibs.2023.08.004.
[24] R. Gibbons, S.A. Adeoya-Osiguwa, L.R. Fraser, A mouse sperm decapacitation factor receptor is phosphatidylethanolamine-binding protein 1, Reproduction (Cambridge, England) 130 (2005) 497–508, https://doi.org/10.1530/rep.1.00792.
[25] M. Fujita, T. Kinoshita, Structural remodeling of GPI anchors during biosynthesis and after attachment to proteins, FEBS Lett. 584 (2010) 1670–1677, https://doi.org/10.1016/j.febslet.2009.10.079.
[26] B. Hess, C. Kutzner, D. van der Spoel, E. Lindahl, GROMACS 4: algorithms for highly efficient, load-balanced, and scalable molecular simulation, J. Chem. Theory Comput. 4 (2008) 435–447, https://doi.org/10.1021/ct700301q.
[27] T. Itagaki, Y. Arima, R. Kuwabara, N. Kitamura, H. Iwata, Interaction between cells and poly(ethylene glycol)-lipid conjugates, Colloids Surf. B: Biointerfaces 135 (2015) 765–773, https://doi.org/10.1016/j.colsurfb.2015.08.014.
[28] Y. Bagheri, S. Chedid, F. Shafiei, B. Zhao, M. You, A quantitative assessment of the dynamic modification of lipid-DNA probes on live cell membranes, Chem. Sci. 10 (2019) 11030–11040, https://doi.org/10.1039/c9sc04251b.
[29] P. Vabbilisetty, M. Boron, H. Nie, E. Ozhegov, X.L. Sun, Chemical reactive anchoring lipids with different performance for cell surface re-engineering application, ACS Omega 3 (2018) 1589–1599, https://doi.org/10.1021/acsomega.7b01886.
[30] T.H. Ho, T.T. Nguyen, L.K. Huynh, Formation of lipid raft nanodomains in homogeneous ternary lipid mixture of POPC/DPSM/cholesterol: theoretical insights, Biochim. Biophys. Acta Biomembr. 1864 (2022) 184027, https://doi.org/10.1016/j.bbamem.2022.184027.
[31] J.S. Suk, Q. Xu, N. Kim, J. Hanes, L.M. Ensign, PEGylation as a strategy for improving nanoparticle-based drug and gene delivery, Adv. Drug Deliv. Rev. 99 (2016) 28–51, https://doi.org/10.1016/j.addr.2015.09.012.
[32] W. Fan, H. Peng, Z. Yu, L. Wang, H. He, Y. Ma, J. Qi, Y. Lu, W. Wu, The long-circulating effect of pegylated nanoparticles revisited via simultaneous monitoring of both the drug payloads and nanocarriers, Acta Pharm. Sin. B 12 (2022) 2479–2493, https://doi.org/10.1016/j.apsb.2021.11.016.
[33] F. Zhang, Y. Xia, J. Su, F. Quan, H. Zhou, Q. Li, Q. Feng, C. Lin, D. Wang, Z. Jiang, Neutrophil diversity and function in health and disease, Signal Transduct. Target. Ther. 9 (2024) 343, https://doi.org/10.1038/s41392-024-02049-y.
[34] Y. He, M.M. Sun, G.G. Zhang, J. Yang, K.S. Chen, W.W. Xu, B. Li, Targeting PI3K/Akt signal transduction for cancer therapy, Signal Transduct. Target. Ther. 6 (2021) 425, https://doi.org/10.1038/s41392-021-00828-5.
[35] A. Hassan, C. Aubel, The PI3K/Akt/mTOR signaling pathway in triple-negative breast cancer: a resistance pathway and a prime target for targeted therapies, Cancers (Basel) 17 (2025) 2232, https://doi.org/10.3390/cancers17132232.
[36] K. Zhu, Y. Wu, P. He, Y. Fan, X. Zhong, H. Zheng, T. Luo, PI3K/AKT/mTOR-targeted therapy for breast cancer, Cells 11 (2022) 2508, https://doi.org/10.3390/cells11162508.
[37] D.J. Pithadia, M.J. Heskel, A. Shotayev, S. Davda, R. Durand, D. Cooke, J. Czechowicz, M. Lesh, P. Cornett, K.A. Shimano, E.F. Mathes, I.J. Frieden, B. Apsel Winger, Alpelisib, a PI3Kalpha inhibitor, effectively treats vascular anomalies with diverse genotypes and phenotypes, Blood Vessel Thromb. Hemost. 3 (2026) 100133, https://doi.org/10.1016/j.bvth.2025.100133.
[38] S. Li, W. Mei, X. Wang, S. Jiang, X. Yan, S. Liu, X. Yu, Choline phosphate lipid insertion and rigidification of cell membranes for targeted cancer chemo-immunotherapy, Chem. Commun. 57 (2021) 1372–1375, https://doi.org/10.1039/D0CC08011J.
[39] E. Kolaczkowska, P. Kubes, Neutrophil recruitment and function in health and inflammation, Nat. Rev. Immunol. 13 (2013) 159–175, https://doi.org/10.1038/nri3399.
[40] G.L. Burn, A. Foti, G. Marsman, D.F. Patel, A. Zychlinsky, The neutrophil, Immunity 54 (2021) 1377–1391, https://doi.org/10.1016/j.immuni.2021.06.006.
[41] M.T. Stephan, J.J. Moon, S.H. Um, A. Bershteyn, D.J. Irvine, Therapeutic cell engineering with surface-conjugated synthetic nanoparticles, Nat. Med. 16 (2010) 1035–1041, https://doi.org/10.1038/nm.2198.
[42] K. Augoff, A. Hryniewicz-Jankowska, R. Tabola, K. Stach, MMP9: a tough target for targeted therapy for cancer, Cancers (Basel) 14 (2022) 1847, https://doi.org/10.3390/cancers14071847.